Final Technical Reports

DoE Award No: DE-FE0003859

Development of Metal Oxide Nanostructure-based Optical Sensors for Fossil Fuel Derived Gases Measurement at High Temperature

Program Period:
09/01/2010 to 08/31/2014

Final Report Date
02/13/2015

PI: Kevin P. Chen, email: pec9@pitt.edu, telephone: 412-624-9675, fax: 412-624-8003

Department of Electrical and Computer Engineering
University of Pittsburgh
348 Benedum Hall, 3700 O'Hara Street
Pittsburgh, PA 15261

Abstract

This final technical report details research works performed supported by a Department of Energy grant (DE-FE0003859), which was awarded under the University Coal Research Program administrated by National Energy Technology Laboratory.

This research program studied high temperature fiber sensor for harsh environment applications. It developed two fiber optical sensor platform technology including regenerative fiber Bragg grating sensors and distributed fiber optical sensing based on Rayleigh backscattering optical frequency domain reflectometry.

Through the studies of chemical and thermal regenerative techniques for fiber Bragg grating (FBG) fabrication, high-temperature stable FBG sensors were successfully developed and fabricated in air-hole microstructured fibers, high-attenuation fibers, rare-earth doped fibers, and standard telecommunication fibers. By optimizing the laser processing and thermal annealing procedures, fiber grating sensors with stable performance up to 1100^{o}C have been developed. Using these temperature-stable FBG gratings as sensor platform, fiber optical flow, temperature, pressure, and chemical sensors have been developed to operate at high temperatures up to 800^{o}C.

Through the integration of on-fiber functional coating, the use of application-specific air-hole microstructural fiber, and application of active fiber sensing scheme, distributed fiber sensor for temperature, pressure, flow, liquid level, and chemical sensing have been demonstrated with high spatial resolution (1-cm or better) with wide temperature ranges. These include the demonstration of 1) liquid level sensing from 77K to the room temperature, pressure/temperature sensing from the room temperature to 800C and from the 15psi to 2000 psi, and hydrogen concentration measurement from 0.2% to 10% with temperature ranges from the room temperature to 700C.

Optical sensors developed by this program has broken several technical records including flow sensors with the highest operation temperature up to 750^{o}C, first distributed chemical measurements at the record high temperature up to 700^{o}C, first distributed pressure measurement at the record high temperature up to 800^{o}C, and the fiber laser sensors with the record high operation temperature up to 700^{o}C. The research performed by this program dramatically expand the functionality, adaptability, and applicability of distributed fiber optical sensors with potential applications in a number of high-temperature energy systems such as fossil-fuel power generation, high-temperature fuel cell applications, and potential for nuclear energy systems.

Table of Contents

Papers and Patents:

1. Kevin P. Chen, Zsolt Poole, Michael Buric, and Paul Ohodnicki, "**Fiber optical sensor employing a metal oxide material**", US Patent pending.
2. Kevin P. Chen, Zsolt Poole, Michael Buric, and Paul Ohodnicki, "**Optical Fiber Based SOFC Fuel Utilization Monitoring and Control System**," US Provisional Patent filed
3. R. Chen*, A. Yan*, Q. Q. Wang *, and K. P. Chen†, "**Fiber optic flow sensors for high-temperature environment operation up to 800°C,**" *Opt. Lett*., vol. 39, pp. 3966-3969 (2014).
4. Z. Poole*, P. Ohodlucki, R. Chen, Y. Lin, and K. P. Chen†, "**3D Sub-wavelength refractive index adjusted metal oxides for applications in optical sensing,**" To appear in Proceeding of IEEE Nanotechnology Conference 2014.
5. Z. Poole*, P. Ohodlucki, M. Buric, S. Riyadh, Y. Lin, and K. P. Chen†, "**Block copolymer assisted refractive index engineering of metal oxide for applications in optical sensing,**" *Proceeding of SPIE NanoScience and Engineering Conference*, paper 9161 (2014)
6. R. Chen*, A. Yan*, M. Li*, T. Chen*, Q. Wang*, J. Canning, K. Cook, and K. P. Chen†, "**Regenerated distributed Bragg reflector fiber lasers for high-temperature operatio**n," Opt. Lett. **38**, 2490-2492 (2013)
7. Z. Poole*, P. Ohodlucki, R. Chen*, A. Yang*, Y. Lin, and K. P. Chen†, "**Engineering metal oxide nanostructures for the fiber optic sensor platform**," *Optics Express* **22**, 2665-2674 (2014).
8. T. Chen, R. Chen, P. Lu, Q.-Y. Chen, and K. P. Chen "**Tapered fibre Mach-Zehnder interferometer for simultaneous measurement of liquid level and temperature**," *Electron. Lett.* **47**, 1093-1095 (2011)
9. T. Chen, R. Chen, C. Jewart, B. Zhang, K. Cook, J. Canning, and K. P. Chen, "**Regenerated gratings in air-hole microstructured fibers for high-temperature pressure sensing**," *Opt. Lett*. **36**, 3542-3544 (2011)
10. T. Chen, Q. Wang, R. Chen, B. Zhang, C. Jewart, K. P. Chen, M. Maklad, and P. R. Swinehart, "**Distributed high-temperature pressure sensing using air-hole microstructural fibers**," *Opt. Lett.* **37**, 1064-1066 (2012)
11. T. Chen, Q. Wang, R. Chen, B. Zhang, and K. P. Chen, "**Distributed flow sensing using optical hot -wire grid**," *Opt. Express* **20**, 8240-8249 (2012)
12. T. Chen, Q. Wang, R. Chen, B. Zhang, C. Jewart, K. P. Chen, M. Maklad, and P. R. Swinehart,, "**Distributed hydrogen sensing using in-fiber Rayleigh scattering,**" *Appl. Phys. Lett*. **100**, 191105 (2012)
13. T. Chen, Q. Wang, R. Chen, B. Zhang, Y. Lin, K. P. Chen, "**Distributed liquid level sensors using self-heated optical fiber for cryogenic liquid management,**" submitted to *Appl. Opt*., (2012).
14. T Chen, R Chen, C Jewart, B Zhang, J Canning, K Cook, K. P. Chen, "**Thermally regenerated fiber Bragg gratings in twin-air-hole microstructured fibers for high temperature pressure sensing**," Proc. of SPIE 8028, 802807 (2011).
15. T. Chen, Q. Wang, R. Chen, B. Zhang, and K. P. Chen, "**Active distributed sensing using Self-heated optical fibers**" *CLEO 2012*, paper CM4B.2 (2012).

16. R. Chen and K. P. Chen, "Fiber Bragg grating in air-hole microstructured fiber for high-temperature pressure sensing," *OSA Conference on Bragg grating, Photosensitivity, and Poling*, paper 136790 (2012).

MILESTONE LOG:

Budget Year One:

Milestone I: Successful development of techniques to produce temperature-stable gratings up to 800^{o}C.

Completion Date: **Month 9 Completed**

Milestone II: Successful development of techniques to produce temperature-stable gratings with various functional metal oxides using both sol-gel deposition and sputtering coating techniques (**completed**).

Completion Date: Month 12

Budget Year Two:

Milestone III: Completion of gas sensing measurement on fiber sensors (**completed**).

Completion Date: Month 16

Milestone IV: Successful development of sol-gel infiltration processes to produce 3D metal oxide photonic crystals from photoresist templates. Other coating techniques for metal-oxide deposition will also be evaluated (**completed**).

Completion Date: Month 22

Budget Year three:

Milestone V: Completion of optical characterization and gas sensing measurements on metal-oxide photonic crystals samples at both room temperature and elevated temperature and submission of the topical report. (**Completed**)

Completion Date: Month 26

Milestone VI: Successful synthesis various metal-oxide films on the wall of hollow-core waveguides using dip coating or sol-gel techniques. (**Completed**)

Completion Date: Month 32

Milestone VI: Completion of gas sensing measurements and comparison studies on coated and uncoated hollow core fibers and delivery of the final report. (**Completed**)

Completion Date: Month 36

Reports on Research Outcomes

1: Construction of rapid heating furnace to rapidly heat up the fiber samples

The furnace originally used to characterize optical fiber devices is the Lindberg 3 zone, shown in **Fig 1a**. Each zone is independently controlled by its own West 4100 PID controller. Process variable read-backs and set-point parameters are manually tabulated from the controller displays. Due to the thermal lag of the system, temperature ramping from room temperature to 700 °C could **take hours**. Thus, the laboriously manual operation of data collection and the inherent sluggish thermal response of this system necessitated the need for responsive and autonomous operational characterization of high-temperature stable gratings.

To perform chemical regenerated grating fabrication works and also to perform thermal testing of fiber sensors at high temperature (800^{o}C), a rapid heating furnace is constructed in the first month of the program as shown in Fig. 1b-c.

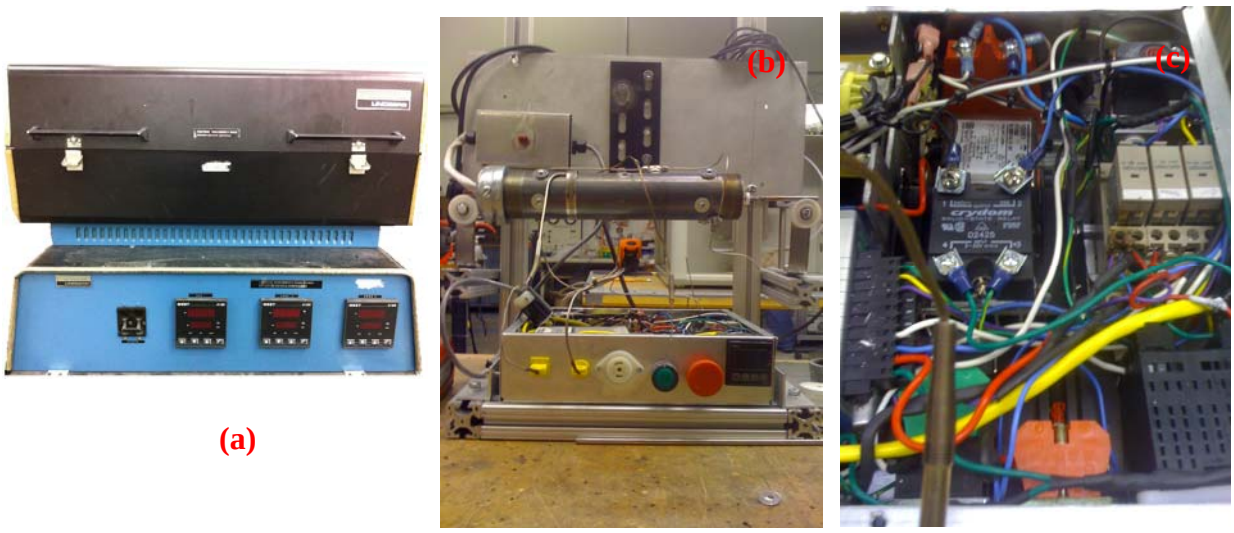

Figure 1: (a) Photograph of Lindberg 3-zone furnace, (b) custom constructed furnace, (c) a close-up photo of the control box.

The furnace is designed and constructed specifically for this project, it utilizes pulse-width modulation technique to control the rapid heating and cooling cycles of fiber samples. Comparing with the commercial furnace we have, the custom-built furnace use less than 200W power. We have developed the entire control hardware (Fig. 1c)

The control software is written in LabView language and can be portable to any other computer running Microsoft Windows XP or higher. Fig. 2a shows the control interface. The furnace has been tested from room temperature to 800^{o}C. Fig. 2a shows the heating and cooling profile under the optimized PID control scheme. The furnace is capable of heating a fiber sample from the room temperature to 800^{o}C under 7 minutes. Using a computer control gas cooling mechanism, it can cool fiber sample down to the room temperature within 10 minutes. The

optimization of the control algorithm will continue to ensure accurate and rapid control of thermal cycle.

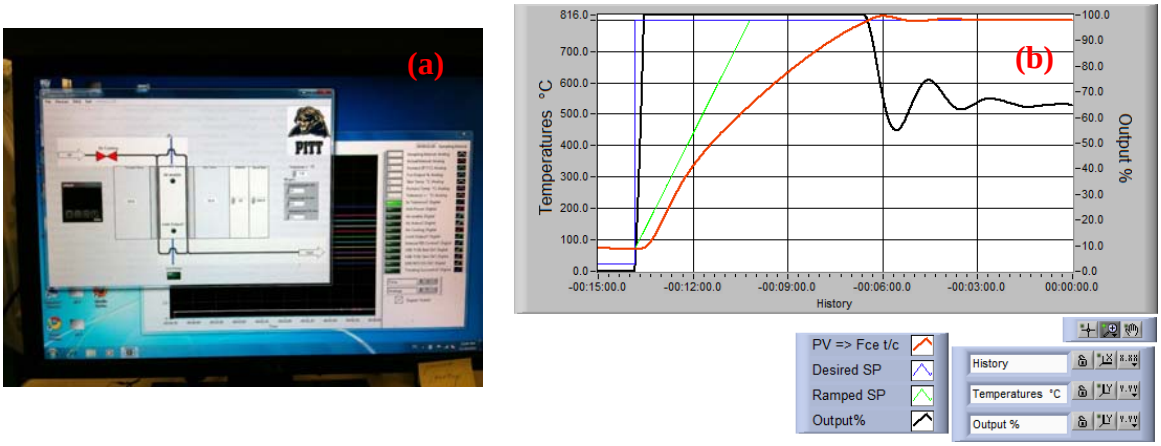

Figure 2: (a) Screen shot of the labview control interface developed for this project. (b) Screen sht of the labview interface showing a test run of the furnace to reach 800°C in 8 minutes.

For high temperature fiber Bragg grating (FBG) manufacturing and testing, the control software recorded the spectral response of the FBG under test through optical spectrum analyzer (OSA) together with the heating log.

A data analysis software is developed to analysis the performance of the rapid heating furnace and the fiber sensors under test. Fig 3 shows the evolution of furnace temperature (in brown), heating duty cycles (in yellow) and surface temperature of the furnace (in pink) over a designed step heating process (in green). The heating log data and optical spectrum data can be easily plot and investigated using this data analysis software. The software also provide a series of data processing functions, including Bragg reflection peak fitting for FBG spectrum, baseline adjustment, and data smoothing.

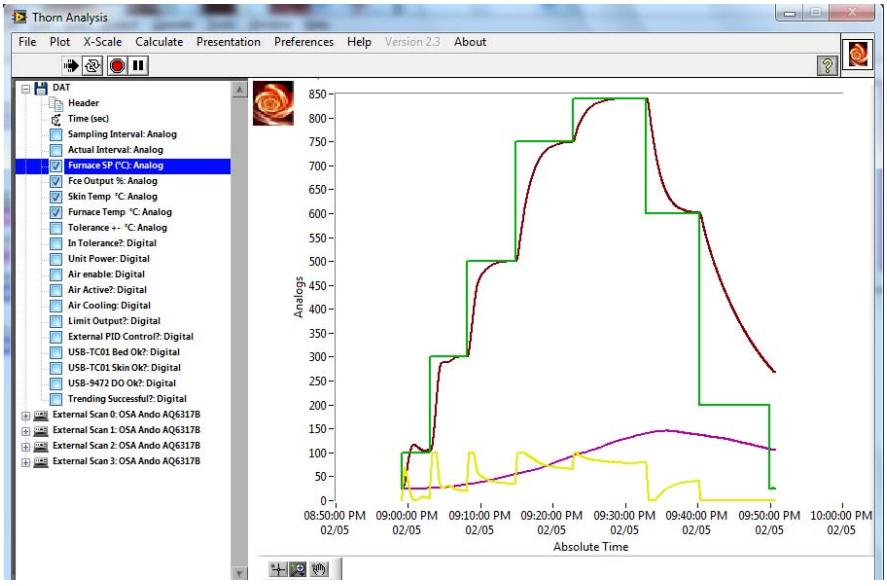

Figure 3: Screen shot of the labview data analysis interface developed for this project.

Using this apparatus, we have tested the thermal evolution of a fiber Bragg grating sample (FBG) written by a KrF excimer laser at 248- nm. Fig. 4 shows the evolution profile of FBG samples as the function of time. The FBG was gradually annealed after 4 hours annealing. The entire spectral data acquisition and furnace temperature control has been automated.

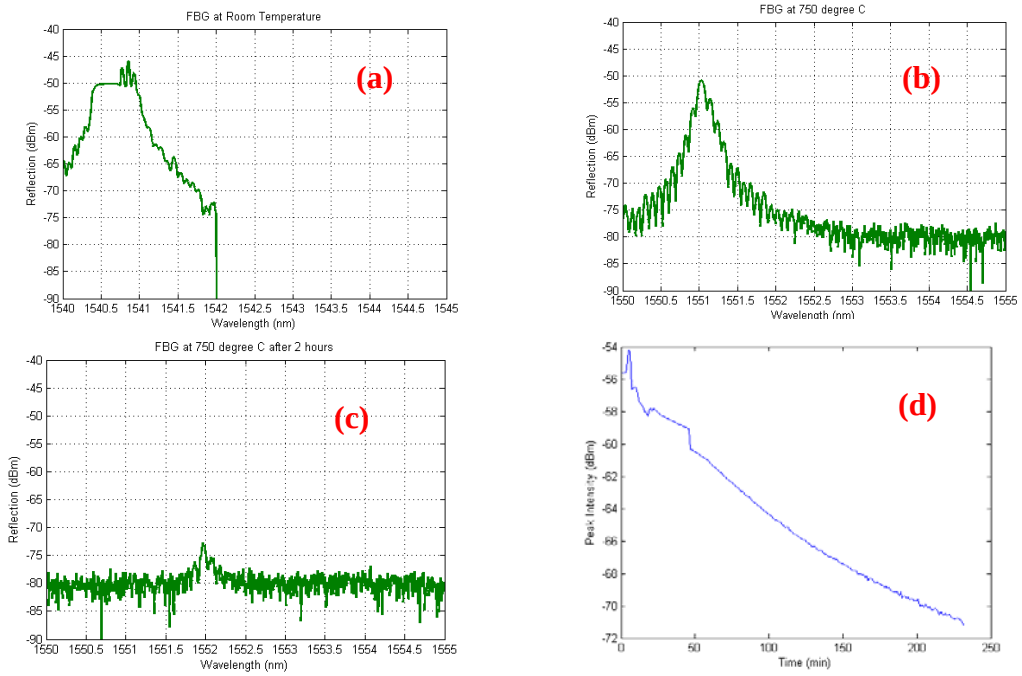

Figure 4: Thermal annealing results for a grating fabricated by a KrF 248-nm laser. FBG spectrum at (a) the room temperature, (b) 750C, and (c) at 800C after 2 hour annealing. The FBG peak evolution at 800C as the function of temperature is shown in (d).

2: Development of High-Temperature Fiber Sensor Platforms

- **<u>High-Temperature Fiber Grating Sensors Produced by Ultrafast Laser Direct Writing:</u>**

Type-II temperature stable FBGs are inscribed point by point into standard communication fibers using ultrafast laser. The thermal experiment was again performed in the same manner as previously mentioned with the temperature being ramped up to a maximum of 1050C in order to monitor the operation near the highest possible point for a silica fiber (1050C) with a grating. The spectral response of the grating can be seen in Fig. 5. The strength of the FBG at 1050C is about 80% of its original value at room temperature. As with the previous temperature run the grating experiences a linear shift with increasing temperature and has a sensitivity of 12.16 pm/C. The FBG strength reduces slightly after 700C. However, it holds stably for two hours at 1050C as shown in Fig. 6b, which highlights the stability of the FBG written by the ultrafast laser.

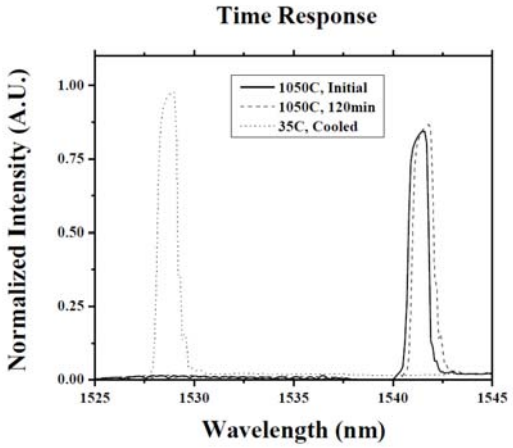

Fig. 5: the spectral response of the ultrafast-laser-written FBG at 35C, 1050C and two hours in 1050C.

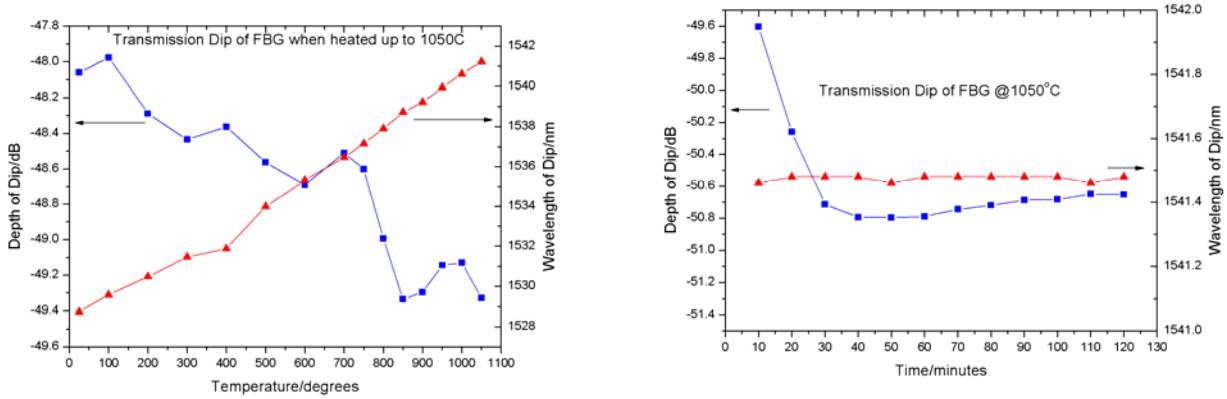

Fig. 6: (a-left) Ultrafast-laser-written type-II FBG in standard telecommunication fibers (SMF-28), thermal response from room temperature to 1050C. (b-right) FBG peak wavelength and strength as the function of time at the annealing temperature of 1050C.

- **<u>High-Temperature Fiber Grating Sensors Produced by Chemical Regenerative Process:</u>**

From the above work, we can see that FBG produced in both standard fibers and air-hole microstructure fibers can sustain temperature as high as 800C. However, the process involves a very expensive laser instruments (i.e. ultrafast laser with mJ pulse output), which is not widely available for fiber sensor fabrication.

Currently, most of FBG sensors were produced by excimer laser, therefore, there is great need to develop fabrication receipts using excimer lasers. In this works, we collaborated with our international partners at the University of Sydney Australia to develop a chemical regenerative processing to produce high-temperature fiber sensor **using the standard telecommunication fiber and standard excimer laser equipment**.

In this work, we also have successfully fabricated regenerated gratings in hydrogen loaded standard fibers using our in-house FBG fabrication facilities. The mechanism of the regenerative process is not very clear, preliminary research carried out by Dr. Canning's group suggests that the process is related to the stress relief in the fiber core. FBG sensors rated for high-temperatures have been fabricated successfully. First Type I gratings were inscribed in standard fibers. Fibers were soaked in hydrogen gas at a pressure of 2000 psi for a week prior to laser exposures. Fiber Bragg gratings were inscribed in hydrogen-loaded fibers by a KrF 248-nm excimer (GSI Lumonics PM244) using a standard phase mask technique. Thermal annealing was applied after the laser exposure at 120°C for 24 hours to stabilize the index change. We have been using this technique to fabricate FBGs and demonstrated several fiber optical sensors with excellent performance for vacuum, pressure, flow and gas sensing.

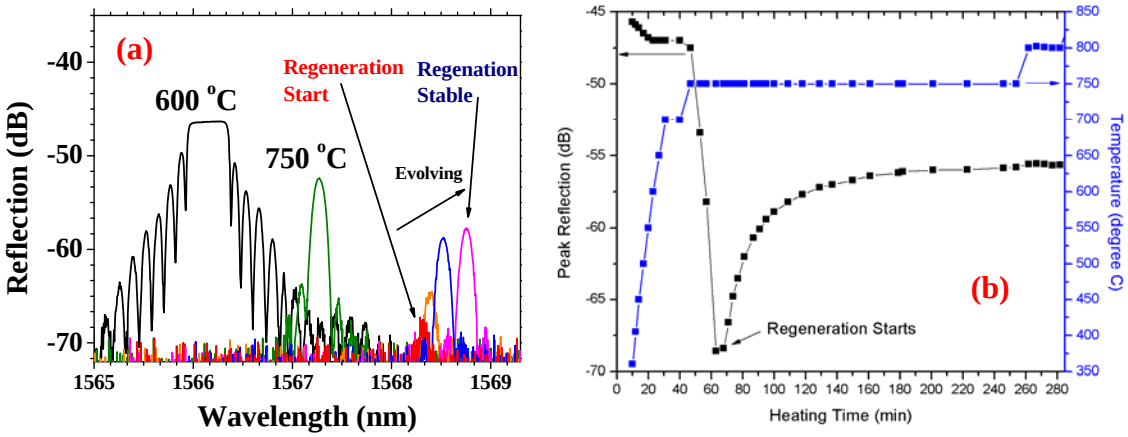

Fig. 8: Temperature stable grating regeneration through thermal annealing: a) The reflection spectra of erasing and regeneration. b) The temperature and the peak reflection as a function of time. The fiber used in this works in Corning SMF-28

The fiber with Type I gratings (referred as seed gratings) was then subjected to a high temperature treatment in a furnace. The grating was *rapidly* heated up to 750°C in 15 min. The reflection spectra of the FBG at 600°C and 750°C are shown in Fig. 8a. The temperature was kept at 750°C and the original peak of the grating was annealed out in about 20 min. The temperature was maintained at 750°C during the regeneration process. The regenerated FBG arise at longer wavelength than that of the seed grating as shown in Fig. 8a. It grew stronger and stabilized after 2 hrs annealing at 750 °C. The regenerated grating was proved to be stable beyond 800°C. The highest operational temperature for regenerative gratings depends on dopants in the fiber core and the regenerative process.

The advantage of the regenerative process is evidence. First, seed gratings were produced using a highly mature UV laser fabrication process. Spectral characteristics of gratings can be carefully controlled and it does not produce large birefringence. The subsequent regenerative process will also produce grating with narrow reflection peaks as shown in Fig. 8a. The well-defined FBG will significantly improve measurement accuracy of pressure-induced birefringence.

To further improve the temperature stability, we performed the regenerative process in high-Ge doped fibers. The thermal testing is shown in Fig. 9. The initial FBG is weak due to the regeneration process. The FBG peak at the room temperature is shown in Fig. 9a. The ramping the temperature up to 900C does not change the shape and strength of FBG as shown in Fig. 9b. However, the FBG diminishes at 1000C.

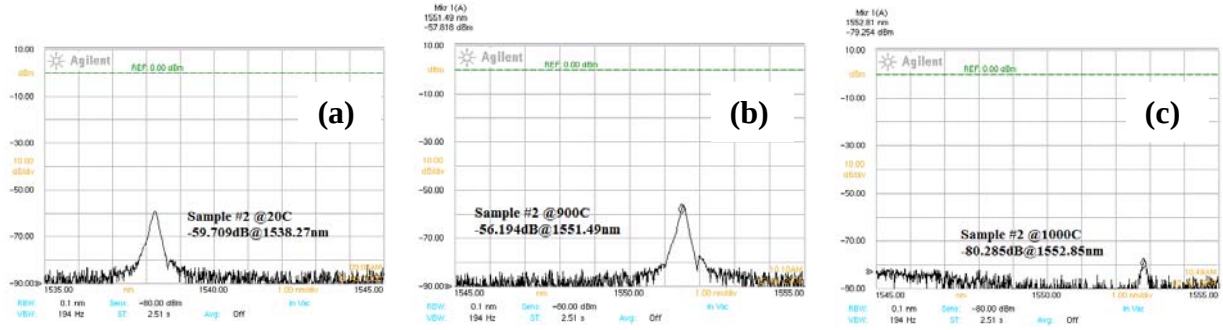

Fig. 9: Regenerative FBG in high-Ge doped fibers at (a) 20°C, (b) 900°C, and (c) 1000°C.

The testing furnace was held at 1000C for over one hour, the thermal degradation was recorded by OSA as the function of temperature and shown in Fig. 10. Fig. 10a shows the FBG peak wavelength and strength as the function of temperature from the room temperature to 1000C. The temperature sensitivity is consistent with 13.1 pm/C as regular FBGs inscribed in SMF-28 fibers. The FBG strength hold steady until 950C and at 1000C, the FBG strength diminish with 40 minutes as shown in Fig. 10b.

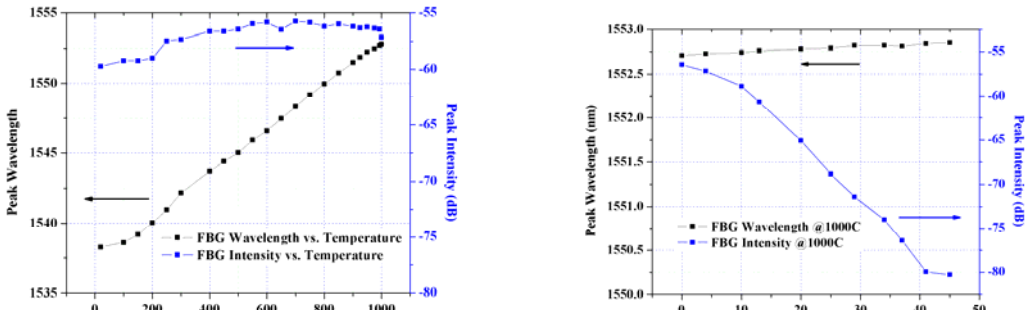

Fig. 10: (a-left) FBG wavelength and intensity vs. heating temperature during an isochronic heating from 20 ºC to 1000ºC. (b-right) the diminishing of FBG intensity and the shifting of FBG wavelength @1000ºC.

The hysteresis of FBG is shown in Fig. 11 for a 6 hour testing cycle. During this test, the testing temperature was ramped from 500C to 900C then back to 500C. Both FBG strength and peak wavelength does NOT show noticeable hysteresis during the testing. This highlights applicability of thermally regenerative grating for high temperature application with the temperature below 900C.

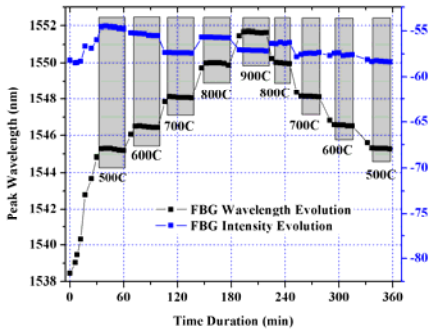

Fig. 11: The 6-hour operation of our high temperature FBG sensor at 500-1000ºC.

In comparison with high temperature FBG produced by the ultrafast laser, thermal regenerative FBGs have much better defined FBG peaks and characteristics for precise measurement. This enables sensing application with better measurement accuracy and resolution. The chemical regenerative FBG can be produced by standard excimer lasers using a phase mask approach. Our test shows that FBG can sustain temperature up to 900C.

In summary, this research project has demonstrated that both the chemical regenerative process and the ultrafast direct writing can be used to produce high-temperature fiber sensors in both standard fibers and air-hole microstructure fibers. They can be produced in large quantities using a phase mask writing technique. Hundreds of such FBG pressure sensors can be multiplexed in a single fiber and serviced by one fiber sensor reading unit using a single fiber feedthrough.

- **High Temperature FBG Sensor using Regenerated Grating in Microstructure Fiber**

During the research period between January 2011 and March 31, 2011, we further extended chemical regenerative FBG fabrication into air-hole microstructural fiber. The air-hole microstructural fibers are a new class of fiber, which allow multi-functional sensor development in fiber. For example, two-hole fiber can be used to measure air pressure and temperature simultaneously. Therefore, our studies on producing FBG in air hole microstructural fibers can be significant.

During the research period ending March 31, 2011, we have achieved extraordinary success on this front! As we will describe here, our approach is superior to those used to produce high-T stable FBG.

Previously, we demonstrated a high temperature pressure sensors inscribed in air-hole microstructure fiber with an ultrafast laser[2]. The type-II FBG shows stable and reproducible sensing operation over 800°C. But the grating linewidth and intrinsic birefringence are wide, which prevent them for better range and accuracy in sensing measurement.

In this period of research, we apply thermal regeneration technique to type-I FBG in air-hole microstructure fiber to produce high-temperature stable grating for pressure sensing. The regenerated grating is stable at 800°C for pressure sensing, and presents **ultrasharp linewidth**

and minimum intrinsic birefringence.

Hydrostatic gas pressure from 15 to 2400 psi is interrogated with the regenerated grating at 800°C, and the sensing resolution can reach 15 psi with a 1-pm resolution tunable laser.

Air-hole fibers used in this work are 220-μm diameter two-hole fibers with two 90-μm air holes as shown in the inlet of Fig. 12a. The fiber core is 9.7-μm × 7.5-μm in size and 4.5-μm away from the geometric center of the fiber. A piece of 20-cm long air-hole fiber was fusion spliced at both end with conventional single-mode fiber (Corning SMF-28). Multiple re-splices were performed to seal the air-holes from ambient pressure. The spliced fiber was loaded in a hydrogen chamber at 2400-psi for 2 weeks, and 3-cm FBG was inscribed into the fiber core with 248-nm KrF laser. Excessive UV exposures were applied in the inscription process in order to obtain strong index contrast, which induced $>10^{-3}$ DC index change and shifted the grating peaks to longer wavelength during the UV radiation. The FBG was then annealed at 800°C, and the evolution of grating in the thermal regeneration process is shown in figure 12a. Blue shift in grating wavelength was observed during regeneration, which is different from previous report on conventional single-mode fiber [3]. This could be due to the gradual relaxation of UV induced DC index in high temperature. Figure 12b shows that both the grating wavelength and strength are stabilized at 800°C 20 hours after the regeneration.

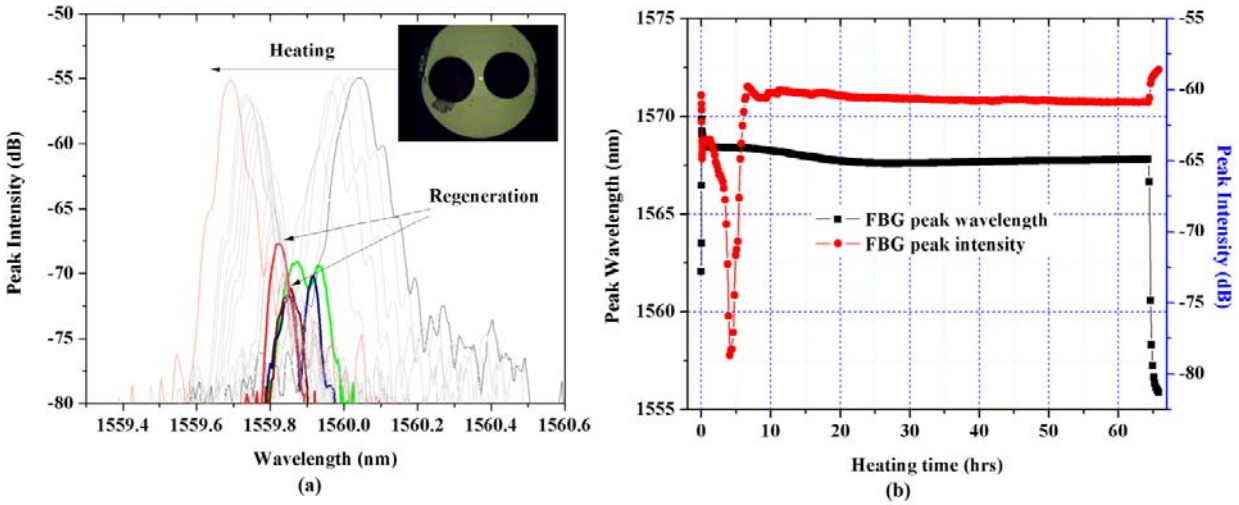

Fig. 12: Evolution of (a) grating reflection spectra, (b) grating strength and resonate wavelength during the regeneration at 800°C. Inset: cross-section image of the twin-hole microstructure fiber under optical microscope.

The hydrostatic pressure testing was performed in a sealed stainless steel tube at 800°C, and the results are shown in figure 13. Under room pressure of 15-psi, the regenerated grating shows a FWHM of <40pm and minimal intrinsic birefringence. When a hydrostatic pressure is applied to the twin-hole fiber, the deformation of the air holes transfers the external pressure into internal stress birefringence in the fiber core, which can be measured by the observation of the grating peak splittings in orthogonal polarizations. Figure 13a shows 180-pm splitting between the orthogonal polarization peaks under 2400-psi at 800ºC, which corresponds to $\sim 1.2\times10^{-4}$ in birefringence. The resonant wavelengths for both polarizations show linear dependences to the external pressure over the entire testing range of pressure, and thanks to the sharp grating

linewidth, the splitting between peaks can be differentiated when the pressure reaches 100 psi. The pressure sensitivity of the grating sensor is 13.3-psi per pm at 800ºC.

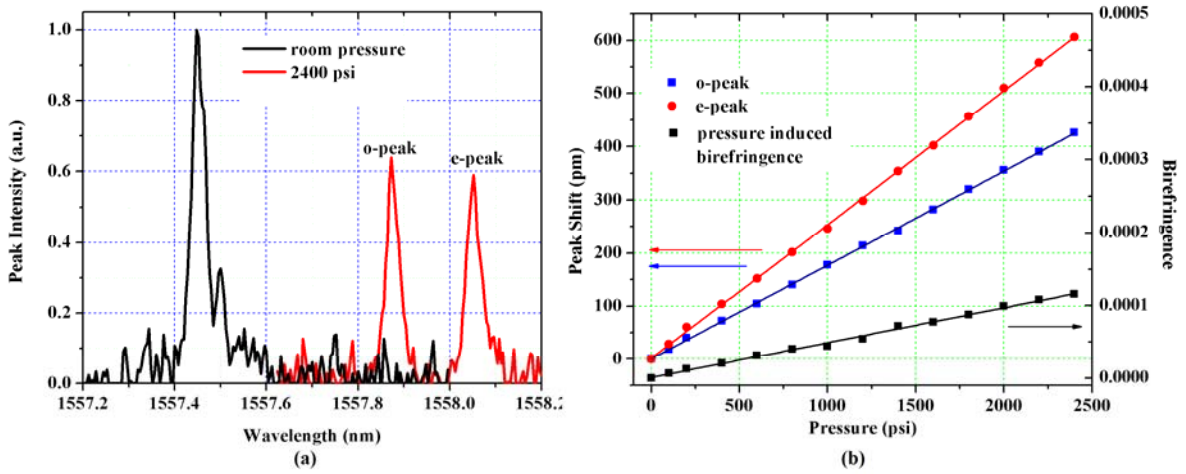

Fig. 13: (a) The reflective spectra and (b) the grating wavelength of the regenerated grating under pressure from 15-psi to 2400-psi at 800°C.

The hydrostatic pressure testing was performed in a sealed stainless steel tube at 800°C, and the results are shown in figure 2. Under room pressure of 15-psi, the regenerated grating shows a FWHM of <40pm and minimal intrinsic birefringence. When a hydrostatic pressure is applied to the twin-hole fiber, the deformation of the air holes transfers the external pressure into internal stress birefringence in the fiber core, which can be measured by the observation of the grating peak splittings in orthogonal polarizations. Figure 13a shows 180-pm splitting between the orthogonal polarization peaks under 2400-psi at 800ºC, which corresponds to ~1.2×10^{-4} in birefringence. The resonant wavelengths for both polarizations show linear dependences to the external pressure over the entire testing range of pressure, and thanks to the sharp grating linewidth, the splitting between peaks can be differentiated when the pressure reaches 100 psi. The pressure sensitivity of the grating sensor is 13.3-psi per pm at 800ºC.

Discussion and Summary

The maximum pressure used to test the FBG sensor was limited by our N_2 tank pressure. It is believed that air-hole silica fiber has potential to sustain much higher pressure up to 10,000-psi according to our simulation. The tested temperature of 800 ºC is also limited by our homemade pressurized high temperature furnace. It is reported that with optimized fiber doping level and annealing recipe, the regenerated grating can survive in temperature as high as 1295ºC[4]. In comparison with the type-II FBG inscribed by the ultrafast laser, better measurement sensitivity and accuracy, and better multiplexing capability can be achieved with the sharp linewidth and minimal laser-induced birefringence of the type-I regenerated FBGs.

In summary, during this period, we apply the thermal regeneration technique to produce high-temperature stable FBG sensors for industry applications. The sensor shows accurate and reliable operation at 800ºC for hydrostatic pressure from 15-2400 psi. In comparison with other fiber optical pressure sensors, the regenerated type-I FBGs in air-hole microstructured fibers are easily multiplexable. A pressure sensing network can be formed with large numbers of these sensors on a single fiber feedthrough, and interrogated with a single optical sensing unit.

3: Development of Functional Coating for Chemical Sensing Using Sputtering Techniques

To coat high-temperature fiber grating sensors with functional materials for chemical sensing, two approaches are being adapted in this program: sputtering coating and sol gel technique. The sputtering coating technique was first tried. In this program, we utilize a sputter coating machine in Lakeshore Cryotronics Inc to coat fiber. Photographs of the jig developed for semi-uniform coating using a standard planar magnetron are shown in Fig. 14. The description "semi-uniform" is applied because the most efficient method right now is to deposit from four directions at 90°. The problem with the planar magnetrons is that the coating adherence and morphology vary with incident angle, and the coating near the edge of the semi-cylinder facing the magnetron might be poorly adhering or granular. The jig was lowered through the load lock gate valve and then picked up and transferred to the sputter station with a horizontal manipulator and clipped in place. The horizontal manipulator was also used to rotate the fiber between depositions.

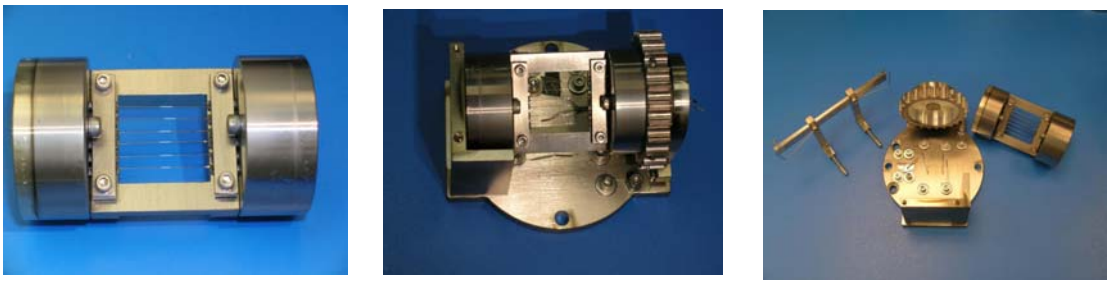

Fig. 14: Components of fiber sputter coating jig. (Left) hanger; (center) carrier plate and rotation wheel; and (right) fiber holder drum. Wire clips on carrier plate hold flat substrates used as witness samples to measure metal thickness.

Utilizing the sputtering coating technique and jigs shown above, we have successfully coated Pd film uniformly on fiber with good adhesion properties. Fig. 15 shows the SEM photo of a coated fiber. This process is under refinement and optimization. The sensing results utilizing these coated fiber is reported in the next session.

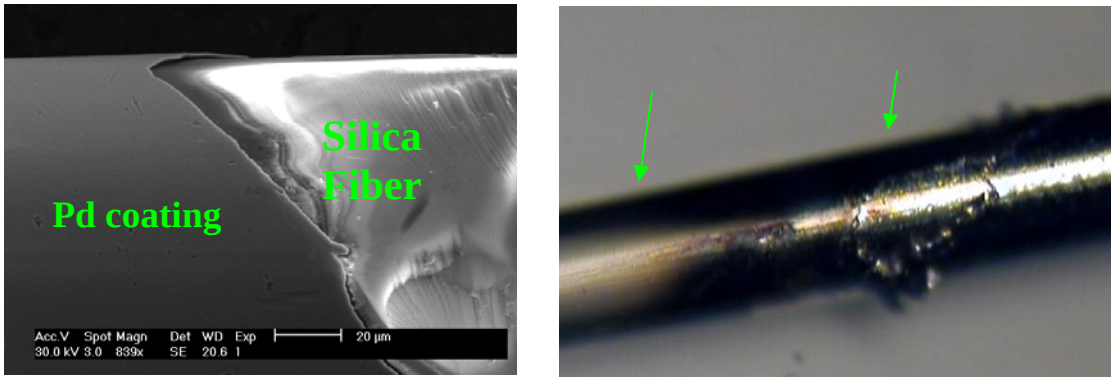

Fig. 14: (left) SEM photo showing the boundary between Pd-coating and silica fiber, (right) Optical microscope photo showing Pd coating.

4: Distributed Fiber Chemical and Pressure Sensors for High-Temperature Applications with millimeter spatial resolution.

The major accomplishment achieved for Report Period # 4 (April 1, 2011 to July 31, 2011) is the first ever demonstration of active distributed fiber sensing technique. Through the fusion of optical frequency domain reflectometry (OFDR) and active fiber sensing scheme, we have demonstrated high temperature fiber sensing and chemical sensing with millimeter spatial resolution.

We believe this is a major achievement for sensor community.

Technical approach of our active fiber sensing scheme is shown in Fig.15. Our approach exploit the exciting opportunities offered by air-hole microstructured fibers and functional fiber coating in pure silica fibers. Through ingenious design, air hole matrices were incorporated into optical fiber, which allows multi-functional measurement. Using Optical Frequency Domain Reflectometry (OFDR) technique to measure the Rayleigh scattering in fiber, every point on a fiber (with a resolution of millimeters) is a sensor. This will provide entire view of power system with unprecedented spatial resolution. Using this combined approach (air-hole fibers + Rayleigh scattering), **every single point on the fiber cross-section (for multi-parameter measurements) and along the entire length of the fiber (for high spatial resolution measurements) can be used as sensors**.

One of the important advantages of fiber sensing is its capability of perform measurement at multiple points along a single fiber. This is achieved by the inscription of in-fiber sensor such as fiber Bragg grating. High spatial resolution can be achieved using FBG sensor array, but the distributed sensing capability is limited by the number of gratings that can be multiplexed and the fabrication costs.

To improve spatial resolution of the measurement, other distributive sensing schemes were developed, which use optical fiber itself as sensor. Being a perfect silica waveguide, fiber can also be used as a distributed sensing device without any modification. The temperature and strain induced refractive index changes along the optical fiber can be interrogated using different techniques including Raman, Brillouin and Rayleigh scattering. In Raman and Brillouin scattering fiber sensing, optical time domain reflectrometry technique (OTDR) is usually employed, in which the system is probed by fast laser pulses and the spatial resolution is limited by the pulse duration. Typically, optical pulse at 1 GHz was used, which lead to typical spatial resolution of OTDR around 1 meter. Very recently, using dual-pulse OTDR technique Optical time domain analysis, the state-of-the-art of Brillouin scattering distributive sensing reaches 12 cm spatial resolution and 28-με strain sensitivity. It is still far worse than FBG sensor.

Rayleigh scattering is the elastic scattering of light by subwavelength-size particles during light propagation. In optical fibers, the density fluctuations of silica material give rise to the Rayleigh scattering loss, which is the fundamental loss limit of optical fibers. The Rayleigh scattering coefficient in optical fiber can be estimated as [1]:

$$\alpha(z)_{Rayleigh} = \frac{8\pi}{3\lambda^4}[n(z)^8 p^2](kT_f)\beta$$

Where *n(z)* is the refractive index profile, *p* is the photo-elastic coefficient, *k* is the Boltzmann constant, β is the isothermal compressibility, and T_f is the fictive temperature at which the density fluctuations are frozen. Rayleigh backscatter in optical fiber is caused by random fluctuations in the index profile *n(z)* along the fiber length. For a given fiber, the scatter amplitude is a random function of distance. However, the Rayleigh back scatter amplitude at a given point *z* on the fiber is a static and deterministically associated with the local structure and density of silica, which can be modeled as a very weak and long FBG with random period as shown in Fig. 8a. When external stimulus (*T, P, strain*) changes the local index, it changes the local reflection spectrum, which can be used as sensing signal.

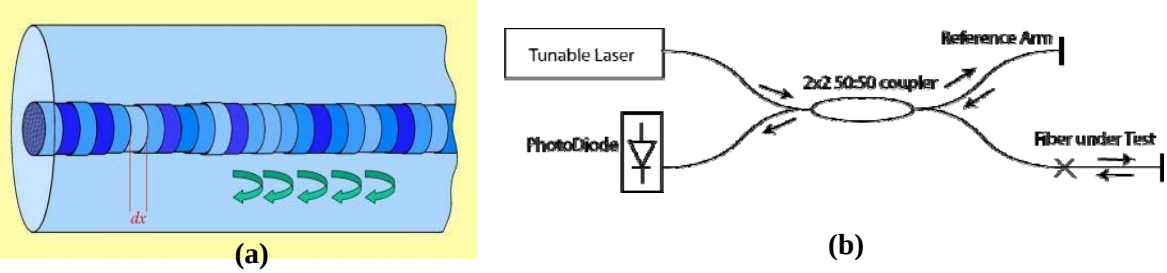

Fig. 15: (a) Schematic illustration of Rayleigh scattering [2], (b) schematic sketch illustration of the OFDR operation principle.

Moreover, contrary to the cases in Raman and Brillouin scattering, the high special resolved optical frequency domain refrectrometry (OFDR) can be applied in Rayleigh scattering measurements in optical fiber. The OFDR technology does not rely on fast laser pulse, rather, it relies on high resolution tunable diode laser and sensitive photo-detection technology, which are commercially available.

The heart of the OFDR technology is a Michelson interferometer shown in Fig. 15b. A highly coherent CW laser is linearly swept from λ_0-$\Delta\lambda/2$ to λ_0+$\Delta\lambda/2$ and coupled through a 2x2 50:50 bidirectional fiber coupler into the reference with length of *L* and the fiber under test (FUT). The reflections from Rayleigh backscattering signal in the test arm and the reference arms are coupled back through the same fiber coupler and mixed at the photodetector.

At the location x of the test fiber, phase difference between Rayleigh backscattered signals at location *x* and reference arms is $\phi(x)=4\pi n(x-L)/\lambda$, where *n* is effective index of the fiber. When the laser is swept from λ_0-$\Delta\lambda/2$ to λ_0+$\Delta\lambda/2$, the AC current at the photodetectors is given by the interference between the reflection from the location *x* and the reference arms and is proportional to $\cos[4\pi n(x-L)/\lambda]$, which is a beating signal with a beating frequency uniquely determined by the location *x* at testing arm. The magnitude and the phase of the beating signal can be used to gauge the change of local Rayleigh scattering, which can be related to refractive index changes.

The spatial resolution of the measurement is directly related to the spectral bandwidth of the frequency scan as [3]:

$$\Delta z = \left(\lambda_0 - \Delta\lambda/2\right)\left(\lambda_0 + \Delta\lambda/2\right)/2n\Delta\lambda$$

For example, 20μm spatial resolution is available with a scanning range from 1535nm to 1575nm [2-4]. However, due to weak reflection signal, integration over longer piece is necessary, which leads to spatial resolution on the order of a few millimeters.

To extract the index change information for both *x* and *y* directions of multiple cores, a modified version of OFDR is proposed as in Fig. 15. The input scanning light is firstly aligned with the slow axis of the system with a polarization controller. The polarization state is monitored at 10% port with

polarized beamsplitter and two channel photodiodes. 90% of the slow-axis polarization maintained light is selectively coupled into the fiber cores with *1xN* fiber optic switch and *Nx1* fan-out waveguide. After going through the fiber core under test and experience local index changes in the slow axis, the input scanning light hits a Faraday mirror, which rotates the beam polarization by 90º. So in the returning trip, local index changes in the fast axis can be interrogated by the scanning light. Finally the fast axis polarized light is collected by the photodetector in OFDR system behind a polarized beamsplitter. After a single scan and Fourier transform, the local index change information in both slow and fast axis can be extracted from the backscatter trace vs. distance, which is symmetric around the Faraday mirrors. Multiple cores can be interrogated in sequence with the optical switch. And multiple parameters including temperature, pressure and 3-D stress can be extracted from a single fiber with millimeter resolution.

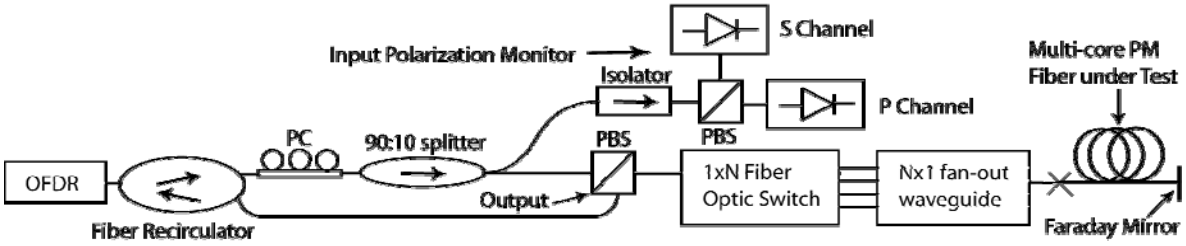

Fig. 15: Block diagram of distributed Rayleigh scattering sensing system for multi-core polarization-maintained fiber.

In this program, we performed comprehensive studies of distributed sensing at high temperature. To perform multi-parameter testing, a two-hole microstructured fiber was used to perform simultaneous high-temperature pressure and temperature measurements at 800C. Since these fibers have been used before, a head-to-head comparison can be carried out to gauge the performance of distributed sensors with FBG sensors. The actual high-temperature testing is performed using a tube furnace as shown in Fig. 16, a commercially available Rayleigh scattering OFDR system were used to perform the back scattering measurement. The polarization of output tunable laser is controlled by an inline fiber polarizer, a 3-zone tube furnace is used to heat a stainless steel tubing. The fiber under test is sealed in the tube, which can be pressurized up to 2200 psi using a nitrogen tank.

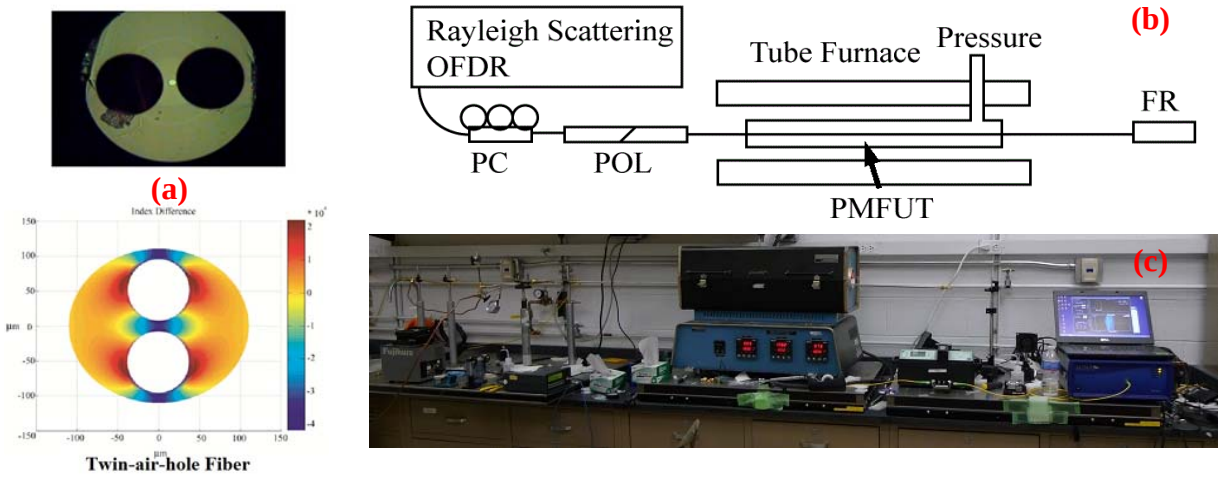

Fig. 16: (a) optical microscope photograph of two-hole optical fiber, the finite element analysis (FEA) simulation of pressure-induced birefringence under 200 bar gas pressure is shown below. (b) Schematic sketch of OFDR experiment setup, a simplified version of Fig. 15. The actual experimental setup is shown in (c).

The Rayleigh back-scattered OFDR experiment is performed in two-hole fibers as shown in Fig. 16a. To simultaneously measure the OFDR signal from both polarizations in order to measure gas pressure at high temperature, an inline polarization controller was used to control the polarization of the input laser. To ensure a high back-scattered signal-to-noise ratio, an inline Faraday rotator was used to flip the polarization at the fiber output, this eliminates the backscattering from the fiber end. Fig. 17 shows an overall OFDR results, the high spatial resolution measurement of OFDR signal can clearly reveal the discontinuity in the fiber path.

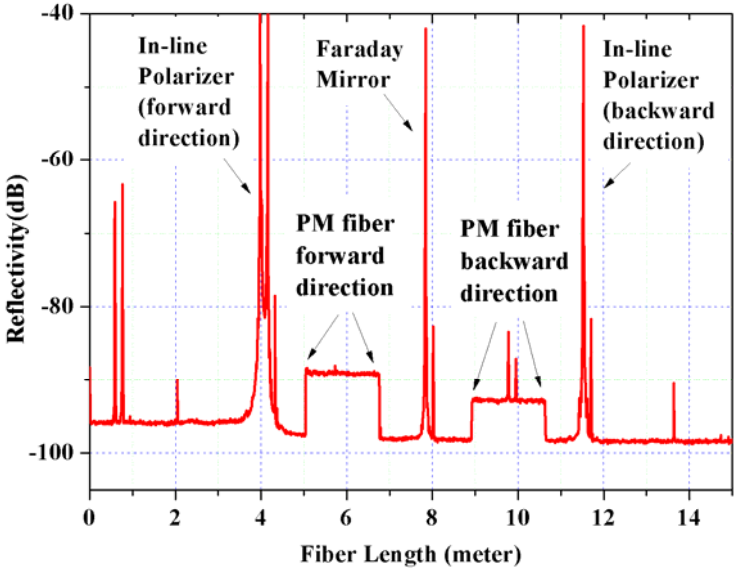

Fig. 17: A typical Raleigh back-scattered OFDR measurement of the two-hole fiber under test. The section of the fiber under test is between 5 and 7 meters, their back-scattering is between 9 and 11 meters, at room temperature.

In Fig. 17, we can see the Rayleigh back-scattered OFDR signal before and after the light passes through the Faraday mirror in two-hole fibers along the fast axis of the fiber. It therefore yields two smooth and uniform Rayleigh scattering signal between 5 and 7 meters and between 9 and 11 meters. To measure the gas pressure, Rayleigh scattering signal from both polarizations have to be measured, this is accomplished by change the polarization state of the inline polarizer. Fig. 18a shows the OFDR measurement response of two-hole fiber under 2000 psi pressure at the room temperature. The differentiation of the pressure-induced strain between two polarization states is clearly visible.

More importantly, the measurement shows a continuous pressure measurement along the two-hole fiber without the need for FBG inscription. This is the major benefit.

- First, costly FBG inscription is not needed, the high-temperature stability of FBG sensors are not of concern any more.
- Further, this approach enables the **high spatial resolution** measurement as demonstrated in Fig. 18a. Using this method, we have achieved a pressure measurement with **better than 1mm spatial resolution**.

Fig. 18b shows the high temperature response of two-hole fiber under the same 2000 psi pressure and 800C. Since there is only one zone in the furnace was used to heated up the fiber, therefore only one section of 2 meter two-hole fibers were heated shown in Fig. 18b between 4200mm and 4700mm.

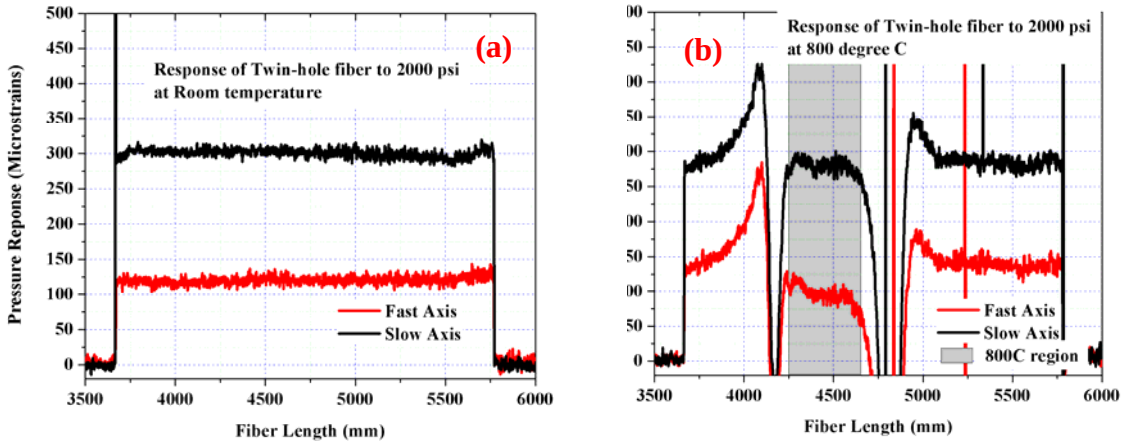

Fig. 18: (a) Rayleigh backscattering signal responses from both fast and slow axes of the two-hole fiber under 2000 psi pressure at the room temperature. (b) The same response at 800C.

Both room temperature and high temperature measurement results as shown in Fig. 18 indicate ~180 με under 2000 psi pressure. We can compare these results with the results obtained by FBG as shown in Fig. 13a, while 2000 psi induced a 180 pm FBG peak split between the fast and slow axes, which is equivalent to a pressure-induced birefringence of 0.18×10^{-3}, this is consistent with the pressure induced strain different measured using the Rayleigh technique (Fig. 18 a-b). A similar sensor response as the function of the pressure is shown in Fig. 19 at high temperature.

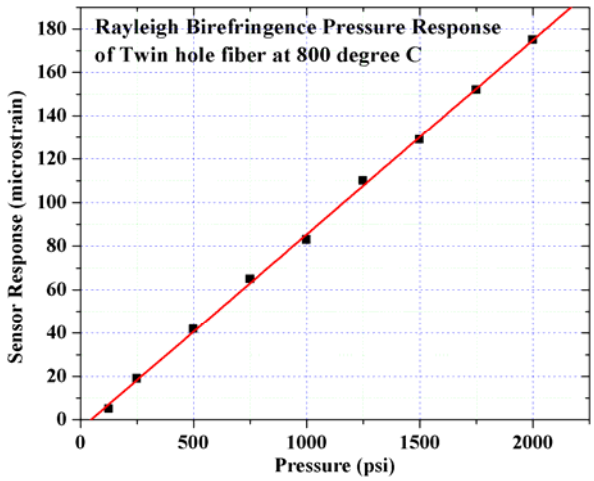

Fig. 19: pressure response of two-hole fiber sensor at 800C.

Both results of Fig. 18 and 19 fully validate our distributed sensing technique using the air-hole microstructured fiber for high temperature sensing without the fabrication of ANY IN-FIBER SENSOR.

Distributed Chemical Sensing: Another major progress we achieved over this period is the first-ever demonstration of distributed chemical sensing using OFDR technology. Using functionally coating on a bare fibers without any in-fiber sensor, we have demonstrated effective hydrogen sensing with better than 1-mm spatial resolution. The experimental setup is shown in Fig. 20.

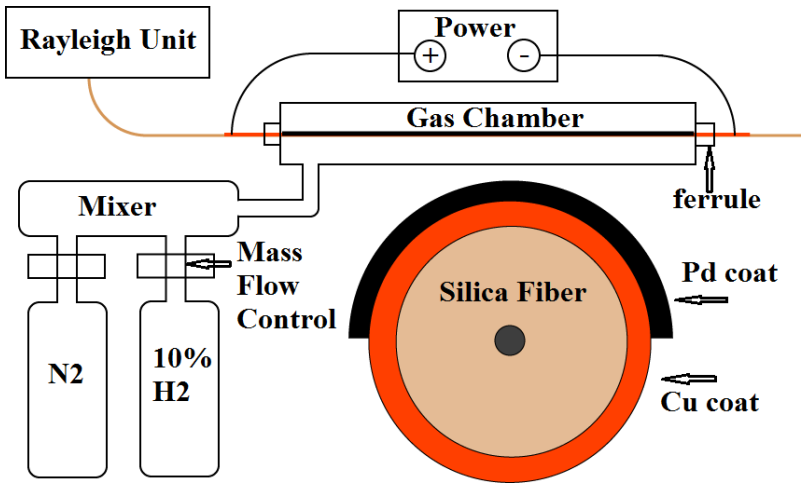

Fig. 20: distributed hydrogen sensing experiments.

To apply hydrogen-sensitive *Pd* film on fiber, the fiber was first coated with ~1 μm thick copper film. This is followed by a sputtering coating of Pd film with a thickness of 200-nm. The mimic different hydrogen concentration along the fiber, the Pd film was intentionally coated about 50% of the fiber with thickness variation along the fiber, which ensure different sensing response of the film even in the same hydrogen concentration. The other important utility of the copper coating is that the fiber can be electrically heated to accelerate Pd-H reaction. The principle of the Pd-based hydrogen sensing is based on Pd-H reaction for the hydride formation. When hydride is formed, the metal film swells, which stretches the fiber and can be measured by the Rayleigh scattering technique.

Once the sensor preparation is complete, the fiber is inserted into the gas chamber. The chamber is fed with 10% hydrogen, the hydrogen concentration can be diluted by another nitrogen tank as shown in Fig. 20.

The first try of our chemical sensing experiment is to test the performance of the Pd-coated fibers. Fig. 21 presents the preliminary test of the Pd-coated fiber using Rayleigh-OFDR measurement unit. During this test, electrical current is supplied to the copper metal coating to heat up the fiber. The no-uniform Pd-film coated outside the copper coating change the local resistivity of the fiber, thus introduce the different temperature profile along the fiber. This is clearly visible in Fig. 21.

The entire testing fiber length, between two fiber ferrules is ~300mm, which will be used to test for hydrogen sensing measurement. The Rayleigh scattering measurement unit is set to measure the strain or temperature induced local index change with the spatial resolution set as 100 μm. The temperature variation caused by coating imperfection is clearly visible. Using the

electrical heating approach, the metal-coated fiber can be efficiently heated up to 140°C, above the phase transition temperature point of Pd metal film.

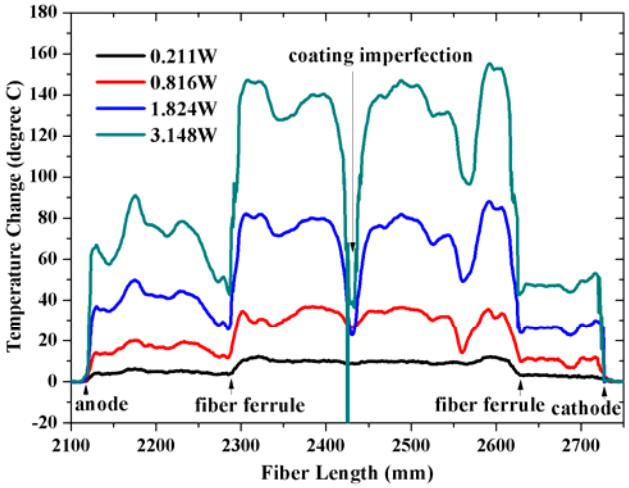

Fig. 21: The temperature profile measurement using OFDR on electrically heated fiber, the Pd coating is between 2300mm and 2630mm

Fig. 22 shows the distributed chemical sensing measurement using Pd-coated fiber. Fig. 22a depicts the 10% hydrogen response of the fiber at the room temperature. The electrical heating was applied to accelerate the sensor response. A 120-second electrical heating enhanced the sensor response up to 3 times. Fig. 22b shows the hydrogen response under 1, 4 and 10% hydrogen concentration. It is evident that the sensor response saturated at 10% of hydrogen. These results are similar to what has been reported in Pd-coated FBG sensor. Both Fig. 22 a-b shows that the location-dependent hydrogen responses, which is attributed non-uniform Pd-coating across the fiber, however, we have not performed optical microscope studies to relate the point-by-point Pd-coating non-uniformity to hydrogen response as measured.

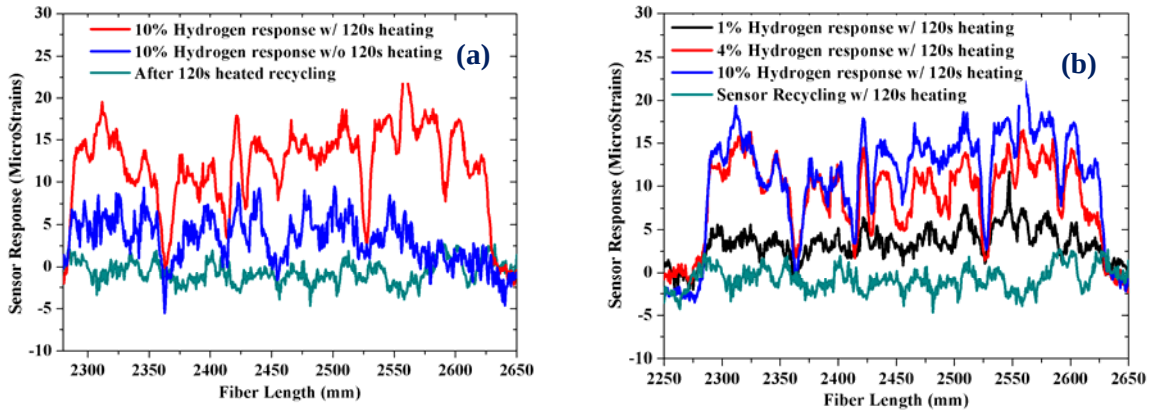

Fig. 22: (a) Distributed hydrogen sensing measurement at 10% hydrogen, fiber response with and without electrical heating. (b) Distributed hydrogen sensing measurement at 1, 4, and 10% hydrogen.

Fig. 23 presents the average response of Pd-coated fiber (in the unit of με) as the function of the hydrogen concentration. It is clear that electrical heating of Pd-coating accelerate Pd hydride formation and thus enhance the sensor response. This is consistent with the Pd-based FBG sensor performance reported in the literature [5] (performed by the PI and using the same coating approach). Our research works performed over this period fully validate the concept of distributed chemical sensor using OFDR technology.

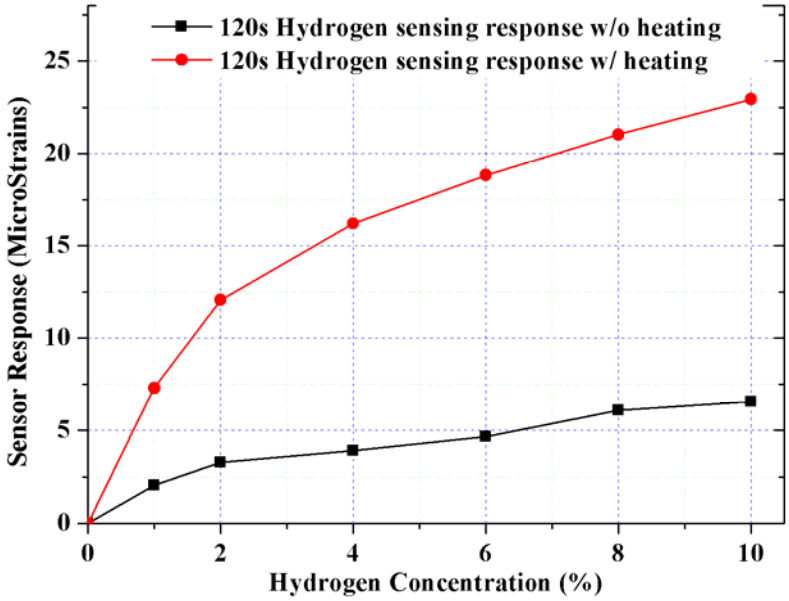

Fig. 23: Sensor response as function of hydrogen concentration.

5. Engineering Metal Oxides Nanostructures for Fiber Optical Sensor Platforms

Metal oxides, amongst their many applications, are an important class of functional materials for chemical and bio sensing. Since the discovery of the sensing properties of these materials, a large variety of metal oxides and their doped variants have been extensively explored for highly sensitive conductometric sensors. [1-5] The basic origin and form of the resistivity response of chemiresistors can be linked to a change in free carrier concentration or free carrier mobility due to the charge transfer interactions that take place between the surface of the sensor and the chemisorbed species.[4] The optimization of the sensors selectivity, sensitivity, and response time to a specific analytes can still pose challenges to many of which doping with impurities does not yield adequate solutions. Nanostructuring metal oxides on the scale of tens of nanometers allow for the tailoring of their fundamental physical, electronic, and optical properties quite extensively for improved sensory performance.[5-13] The increase of the surface area of metal oxide nanostructures enhances the interactions between the oxide and the target species. The typical width of the gas modulated space charge region is between 1 and 10nm; therefore, nanostructuring on the scale comparable with this width provides high ratios between the modulated and non-modulated regions, allowing more effective utilization of the sensing material in comparison with thin film devices where the interacting volume is just the modulated width of its geometric surface.[5, 12, 14, 15]. Lastly, the controlled nanostructuring on the tens of nanometer scale allows the tuning of the dielectric constants of metal oxides at will while maintaining sufficient scale separation between the dimensions of the nano features and the typical operating wavelengths (visible and near infrared, NIR).[13]

In addition to their extensive use in conductometric sensors, functional metal oxide nano-materials are excellent candidates for optical sensor platforms such as optical fiber. As a robust and scalable sensing technology well-suited for harsh environments, fiber optic sensors can provide unique opportunities and can perform in many conditions that are impossible for electronic sensors (e.g. high temperature, corrosive, strong electromagnetic fields, volatile organic/inorganic species). The integration of metal oxides with optical fiber constitutes a unique set of technical challenges. A critical way to improve the sensitivity of fiber optic sensors is to increase the interaction length between the metal-oxide coatings and the guided light. This in turn facilitates the accumulation of the response, whether refractive index or absorption based, leading to an increase in sensitivity. This is not a trivial issue given that the typical refractive index of metal oxides ($n>2.0$) are significantly higher than that of commercial silica fiber cores ($n\sim1.46$). The optical interaction between the cores of silica fibers with higher index sensing films in close proximity can be detrimental to optical guiding.

To date, successful demonstrations of fiber optic sensors utilizing metal oxides are realized by thin film coatings as in this domain the index compatibility issues can be mitigated.[16-22] As a rough estimate, the thickness of the high-index sensing film should be less than ¼ of the wavelength in the metal oxide sensing film ($\lambda/4n$) to preserve guiding in the low-index fiber core.[23] This restriction on the film thickness (typically less than 150 nm) places severe limitations on the interaction volume of the evanescent wave with the sensing medium. A schematic of D-shaped fiber coated with SnO_2 in contact with the fiber core is illustrated in **Fig. 37A**. D-shaped fiber is a choice platform in optical fiber chemical sensing since the fiber core can be accessed while maintaining sufficient structure for mechanical stability. **Fig. 37B** shows the detrimental effects when a high refractive index thick film (2-μm) is coated in contact with the fiber core, where most of the guided light is transferred to the fiber coating and is lost. **Fig. 37C** illustrates the mode power distribution in the device when the refractive index of the film (1.461) is slightly lower than that of the fiber core (1.468), a configuration in which light guiding is preserved.

We explored the dependence of the confinement factors on the film thickness and the refractive indices by finite element analysis. **Fig. 37D** shows this dependence when the condition of mode matching is enforced, when the metal oxide coating does not disturb the guided mode in the fiber core. This is

defined as the fiber maintains a constant effective index ($n_{eff\text{-}sensing} \approx n_{eff\text{-}uncoated}$ =1.464). Simulations indicate that a metal oxide coating with nominal index of 1.9 would require the coating thickness to be 123nm or less, in order to preserve guiding in the D-shaped fiber core as shown in **Fig. 37D**, yielding a confinement factor of 0.29%.

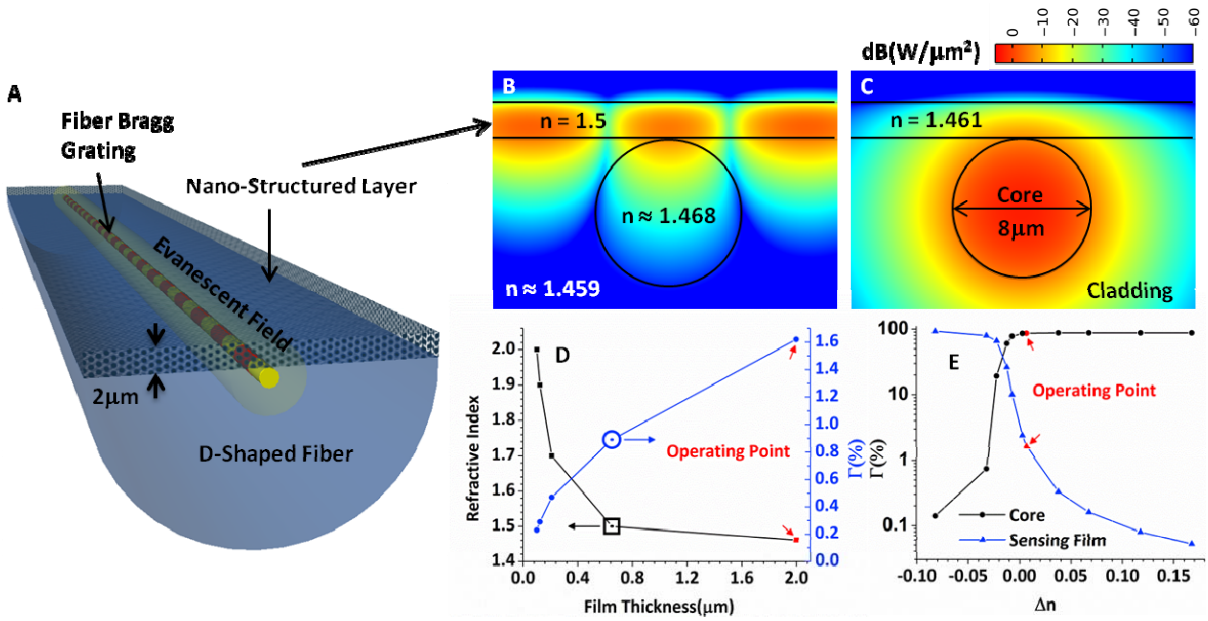

Figure 37: **A**: Schematic of D-shaped fiber coated with nanostructured SnO_2, with an in-fiber Brag Grating. **B-C**: Simulations of the power distributions of the fundamental mode for a coating refractive index of 1.5 (index above the value of the core) and 1.461 (Nanostructured SnO_2 used for the experiment). **D**: Simulations of various coating refractive indices and the associated confinement factors as functions of film thickness while maintaining the mode-match condition. The thicknesses are those that maintain the fiber's n_{eff} to its original value. **E**: The confinement factors as functions of the index difference between the core and the sensing film ($\Delta n = n_{core}\text{-}n_{film}$) at a coating thickness of 2μm for small film index variations. The above simulation were examined for an operating wavelength of λ=1.55μm.

In this report, we demonstrate that the complications and limitations of using metal oxides with high dielectric constants can be overcome by replacing thin film designs with refractive index tailored 3D nanomaterials.[27] The use of a structure directing agent in the wet chemical preparation of SnO_2 provides an engineering opportunity on the tens of nanometer scale where, by controlling the structure directing component, the refractive index can be adjusted in accordance with effective medium theory. Reducing the refractive index below the refractive index of the fiber core removes the thickness constraints, allowing the coating of thick 3D nanomaterials while maintaining mode matching between the sensing and non-sensing regions of the fiber for intrinsic loss optimized designs. This allows the coating of films with arbitrary thicknesses, which greatly enhance the evanescent wave interactions.

The effects of small variations in the refractive index, near the optimal refractive index, on the confinement factors was examined by simulation for a 2-μm thick coating ($\Delta n = n_{core}\text{-}n_{film}$) shown in **Fig. 37E**. When the refractive index of the metal oxide is slightly smaller than that of the fiber core, a 4-10 times enhancement in confinement factor for evanescent wave interaction can be achieved in the sensing films. In addition, the tailoring of the refractive index allows the many previously explored benefits of metal oxide nanostructures to be incorporated into optical fiber sensors such as increased surface to volume ratios and higher ratios between the modulated and non-modulated regions yielding faster and more sensitive sensors.

In the optical domain, it is not easy to predict the type of the expected response or combination of responses for metal oxide nanostructures with features comparable to the gas modulated space charge region's width, for which the surface effects dominate. It is well known that a conduction increase/loss is to be expected, depending on the type of the analyte (reducing/oxidizing) and the type of the metal oxide (n/p-type). This, in the optical domain at NIR, for SnO_2, will show up as absorption based on Drude's theory as in this regime the response is dominated mostly by free electron absorption.[24, 25] Based on the theory, however, it is not clear whether there should be an expected measurable change in the real part of the refractive index. In addition to absorption, a measurable modulation in the real part of the refractive index could potentially provide another method in cross sensitivity discrimination, which is a common problem of metal oxide sensors.[26] To probe the optical sensory mechanisms of the SnO_2 nanomaterial, this paper use a fiber Bragg grating in D-shaped fiber to simultaneously measure the optical losses and the refractive index changes from room temperature up to 500^{o}C in response to NH_3. In this work, SnO_2 was used as an example for refractive index tailoring through controlled nanostructuring. However, we point out that this approach is general and should be transferable to optimizing the response of optical fiber sensors integrated with many metal oxide based materials.

RESULTS AND DISCUSSION

In the wet chemical synthesis of the precursor, Pluronic F-127, a triblock copolymer was used as the structure direct agent for the nano-engineering of SnO_2.[15, 28-30] By controlling its mole fraction, the porosity of the SnO_2 is controlled on the tens-of-nanometers scale to tailor the refractive index of the nano-material. In prior, this method was shown effective towards modifying the resistive and surface properties of metal oxides. The Lorentz single oscillator model along with Bruggeman's effective medium theory was used in the fitting process to estimate the refractive index of the nano-material.

The sol gel solution used in the fabrication of the nanomaterial consisted of $SnCl_4$, Pluronic F-127, HCl, and Ethanol with a molar ratio of 0.0253:0.00105:0.466:1 (ACS Reagent Grade, Sigma Aldrich). After mixing, the solution was stirred for 3 hours, followed by a settling period of 24 hours. In the preparation of the precursors, many authors employ careful humidity control in processing these materials. We found that the hydrolysis can be substantially slowed upon exposure with ambient air by adjusting the pH value of the precursor to ~0.5 using HCl.[29] The slowing of the hydrolysis provided higher quality films when spin coated for refractive index measurements.

To characterize the refractive index, the precursor was spun onto a silicon wafer at 2500 RPMs, heat treated and measured using an Ellipsometer (Jobin Yvon Uvisel Spectroscopic Ellipsometer). The Lorentz single oscillator model along with Bruggeman's effective medium theory was used in the fitting process to estimate the refractive index of the nano-material.[31, 32] Parameters were measured in the range of 400-800nm after which the model was used to extend the refractive indices to 1600nm. Extrapolating the refractive index in this manner should provide reasonable values as it has been shown that the variation in the dielectric constant of SnO2 at higher wavelengths is slowly varying.[33]

Fig. 38 shows the fitted from direct measurement (400-800nm) and extrapolated (800-1600 nm) refractive indices of various form of SnO_2. The refractive index of bulk, fully dense SnO_2 is also presented as a reference (built into the software package of the Ellipsometer). A 100-nm thick SnO_2 thin film prepared by sputter coating (estimated porosity of around 3-5%) is also included for comparison. Refractive index measurements of three nanostructured SnO_2 films are presented in **Fig. 38** with varying contents of Pluronic F-127 (SnO_2 – A, B, and C). We determined a volume fraction of about 60% for nanostructured SnO_2 –B (nanomaterial used in the construction of the sensor). At 1550nm, the wavelength of interest, it has a refractive index of 1.461, which is slightly smaller than the refractive index of the fiber core (1.468).

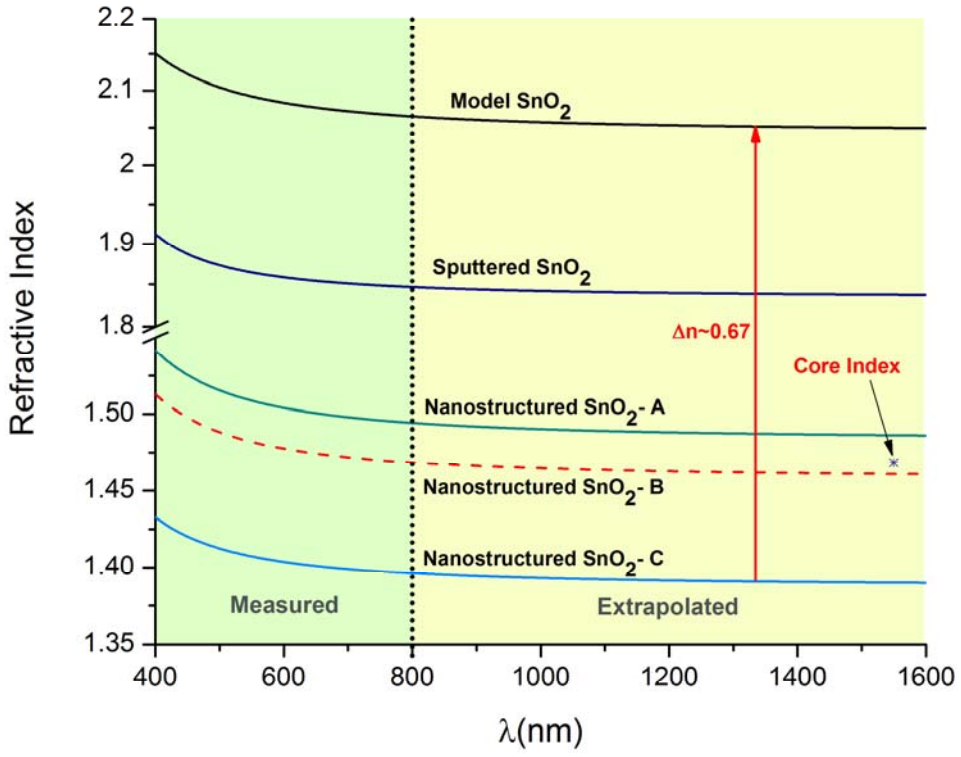

Figure 38: The refractive indices of various forms of SnO_2. Sputtered SnO_2 was sputter coated at a thickness of 100nm. SnO_2-A is with mole fraction 0.046:0.00037:0.25:1, B with mole fraction 0.025:0.00105:0.466:1, and C with mole fraction 0.025:0.00026:0.406:1. The mark labeled "Core Index" is an estimate of the refractive index of the core of the fiber (1.468) and SnO2-B, used to fabricate the sensor, has an estimated refractive index of 1.461 at λ=1.55μm.

A cross section SEM image of the sensor in **Fig. 39A** shows that the thickness of the film directly above the core is roughly 2μm. Sufficiently thick for trapping most of the evanescent energy in the interaction region, as calculations show that greater than 98% of the radiant intensity of the evanescent wave is in the coating. Cross-sectional TEM samples were prepared through standard focused ion beam (FIB) lift-out procedures for SnO_2 deposited on the D-shaped fiber (inset of Fig. 3B). A protective layer of Pt was deposited on the surface prior to sectioning. A tungsten-probe tip was used for sample lift-out and electron transparency was obtained over an approximately 10μm wide region for the entire film thickness. Scanning transmission electron (STEM) images of **Fig. 39B** clearly show a large degree of film porosity through z-contrast with features of about ~20-50nm in diameter. Bright field TEM imaging shows an average SnO_2 grain size of approximately 10nm (**Fig. 39C**) and a Fast Fourier Transform (FFT) obtained from the high resolution TEM image indicates and underlying cassiterite crystal structure (**Fig. 39D**).

To produce the fiber Bragg grating, D-shaped fiber was first soaked in high pressure hydrogen at 1600 psi for 2 weeks. A type II Fiber Bragg Grating (FBG) was inscribed by a phase mask (2.5x1cm with 1060nm period) with a 248nm KrF laser source (GSI Lumonics PM-844) with a cumulative fluence of ~6,000 pulses at ~50mJcm^{-2}.[34, 35] The FBG sensor was then annealed at 120^{o}C for 24 hours to diffuse out all the residual hydrogen. Prior to coating the precursor, the D-fiber with the FBG was etched with a

buffered HF solution for 21 minutes to remove 3μm cladding material (5:1 40% NH_4F to 49%HF ACS Reagent Grade, Sigma Aldrich), exposing the core on the flat side of the fiber. The fiber was coated by pulling it through the precursor at an approximate rate of 0.5cm/s. The coated sample was then exposed to a temperature treatment which started by drying at 80°C for 3 hours. Next, the temperature was increased at 5°C/minute to 130°C and held for 1 hour. Followed by ramping (3°C/minute) to 600°C, where it was held for 2 hours. Afterwards, the sample was cooled to room temperature at a rate of 3°C/minute.

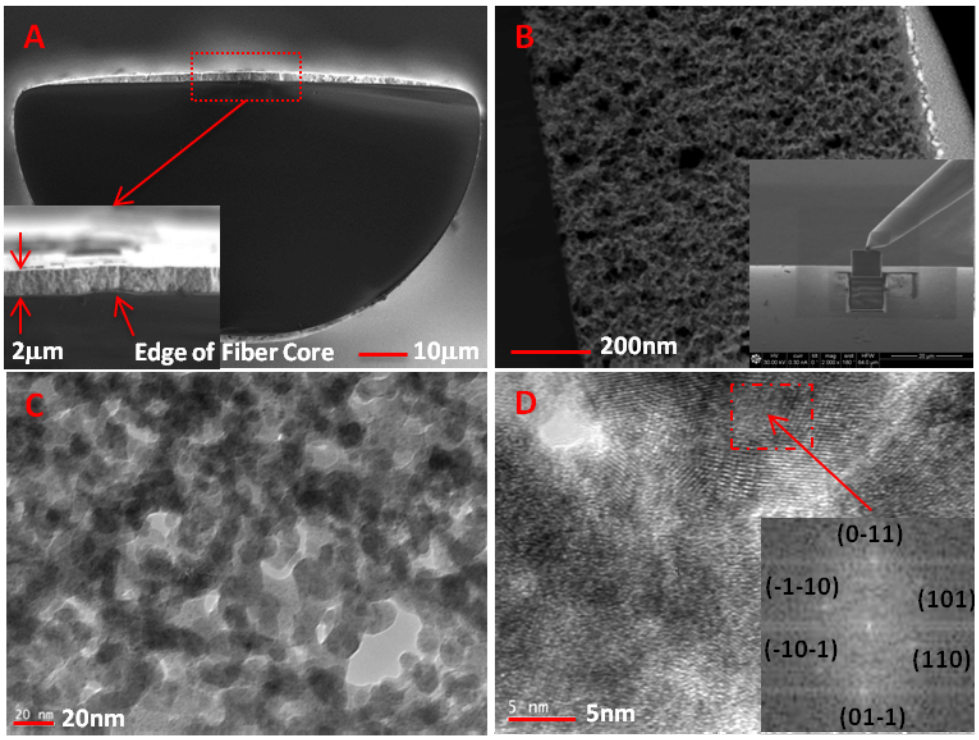

Figure 39: A: Cross sectional SEM image of the constructed sensor. **B:** STEM image of the entire film thickness along with an SEM image (inset) illustrating the FIB lift-out. **C:** Bright field TEM image illustrating an average SnO_2 grain size of approximately 10nm. **D:** High resolution TEM imaging of the crystal structure of SnO_2 with FFT inset indexed to the [1-1-1] zone axis of the casserite crystal structure.

The schematic of the gas sensing experimental setup is shown in **Fig. 40A**. The fiber sensor coated with the reduced index SnO_2 was exposed to a constant flow(200 SCCM) of 10% NH_3 and 90% N_2 mixture at atmospheric pressure for 3 minutes, followed by a 3 minute recovery period in dry air(200 SCCM). A change in the real part of the refractive index of the 7-cm long fiber coating is monitored by the reflection peak of the FBG sensor using a broadband light source (EBS-7210 Er^{3+} Broadband, MPB Technologies) and an Optical Spectrum Analyzer (Agilent 86140B). Another Optical Spectrum Analyzer (Ando 6317B) was used to monitor transmission spectra of the coated D-fiber to measure the real-time optical loss. The FBG reflection peak disappears immediately upon the coating of the precursor due to its high refractive index in comparison with the core of the fiber. A short time after raising the temperature above 200°C, the grating peak begins to return due to the removal the structure directing agent, indicating the reduction of the refractive index.

A change in the effective index Δn_{eff} of the guided mode can be measured directly by monitoring shifts in the FBG peak $\Delta\lambda$ as $\Delta n_{eff} \approx \Delta\lambda/2\Lambda$, where Λ is the grating period.[36-38] Any displacements in the peak under stable temperature conditions, which we could detect down to 10-pm levels, would be indicative of a refractive index change in the nanostructure. An example of the measurement of the

wavelength of the resonant peak is given in **Fig. 40B**, at room temperature. In measuring the reflected power from 25-500°C, we do not observe any shifts in the resonance peak due to the adsorption of NH_3. Given the sensitivity of our instruments and the 1.62% optical confinement factor in the sensing film, we estimate that any modulations in the refractive index is smaller than $\sim 5\times10^{-4}$.

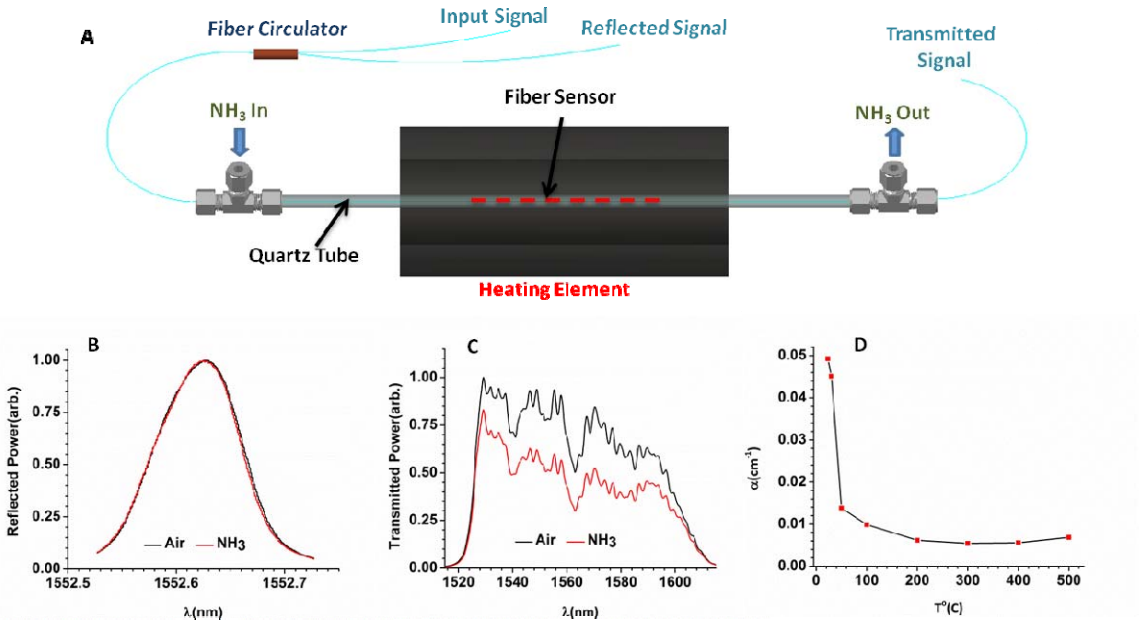

Figure 40: **A:** Experimental schematic. **B:** FBG resonant peak response of the sensor at room temperature to 10% NH_3. No shift in the resonance peak is observed, indicating that there is a not a significant refractive index response. **C:** Transmission analysis of the response of the sensor at room temperature to 10% NH_3, indicating a strong loss in the transmitted power. **D:** The total absorption coefficient of the integrated component as a function of temperature.

The above exposure conditions produce a significant optical loss evident in the transmission measurement, for which we measured about a 30% reduction in the transmitted optical power around 1.5μm (**Fig. 40C**). The optical loss coefficient of the device in this configuration is α_{Sensor}=0.049cm^{-1}. Given that 1.6% of guided light interacts with the metal oxide coating, the overall absorption coefficient for SnO_2 materials in reaction with NH_3 is α_{SnO2}= 3cm^{-1}. The loss appears to be uniform across the transmission measurement spectra. A maximum in the transmitted power was observed at room temperature after which it shortly declined with the increase of the temperature as shown in **Fig. 40D**. This result is contradictory to the general thermal dependence of chemiresistors as their temperature response has a maximum sensitivity at higher temperatures, typically between 200-500C; therefore, many devices tend to hold their SnO_2 sensor in that temperature range for peak sensitivity. On the other than, SnO_2 nanowires have been reported to have thermal characteristics different from their bulk counterpart as do SnO_2 nanoclusters.[6, 7, 39] From this, we speculate that the anomalous temperature response might be due to the current nanostructure.

In summary, work performed in this period presents the effective integration of reduced index nanostructured SnO_2 with the fiber optic sensor platform with a significant improvement (4-10 times) in the confinement of the interaction energy. The refractive index was successfully adjusted by a triblock copolymer, Pluronic F-127 which acted as a structure directing agent in the manufacture of the SnO_2 nanomaterial with a refractive index that is amenable for integration with the optical fiber platform. Furthermore, we have examined a possible refractive index and absorption modulation of the presented

sensor from room temperature to 500^{o}C in the 1550nm wavelength range. The results indicate that exposing the evanescent wave SnO_2 sensor to NH_3 induces much stronger changes in absorption as opposed to changes in the refractive index.

We believe that this work can provide important guidance for the design of optical fiber sensors employing metal oxides as sensory transducers. The weak refractive index modulations indicated by our measurements suggest that index-based fiber sensors such as fiber gratings and in-fiber interferometers might not be suitable sensor platforms for SnO_2 or related metal oxide materials for the detection of gas species. Fiber sensors designed to measure small optical absorption such as cavity ring-down spectroscopy is better suited to harness the strong optical absorption for highly sensitive chemical sensing when integrated with reduced index metal oxide nanomaterials.

6. Regenerated distributed Bragg reflector fiber lasers for high-temperature operation

Fiber lasers are powerful tools for sensing applications. Compared with passive fiber Bragg gratings, active sensing schemes based on fiber lasers normally show superior performance in terms of sensitivity, wavelength resolution, and accuracy. Recent research efforts [1-3] have extended the operating temperature of fiber lasers to 600 °C for high-temperature harsh environments. This is well beyond those prescribed for classic applications such as telecommunications. The successful development of all-fiber high-temperature fiber lasers relies on high-temperature-resistant fiber Bragg reflectors. In view of those requirements, FBGs inscribed by ultrafast lasers, at the first place, have been proved to be promising candidates. For example femtosecond laser inscribed Type II gratings were successfully used in fiber lasers operating at temperature up to 600 °C [1] and output power scaling to 103W [4], thanks to their high-temperature stability and subsequent power handling capability. Conventional UV-inscribed Type I fiber gratings are typically less temperature-resistant than those fabricated by femtosecond lasers. Annealed UV-inscribed fiber gratings in photosensitive fibers, with much simpler fabrication process and less costs, can sustain lasing up to 400 °C [2].

In comparison with the gratings used in previously discussed fiber lasers, thermally regenerated gratings [5-7] are another class of high-temperature-resistant fiber gratings. The thermal regeneration of high-temperature-resistant gratings involves a mechanical relaxation process [8], which is independent from the chemical composition of fibers and hydrogen loading processes. Thus, thermally regenerated gratings can be fabricated in a wide variety of fibers at low cost for extreme environments. Canning *et al* has reported linear temperature and strain responses in thermally regenerated gratings from room temperature to 1100 °C [9], which render regenerated gratings as a significant enhancement to conventional fiber grating applications, especially for extreme environments. Recently, we have demonstrated a regenerated grating based high-temperature pressure sensor, with which hydrostatic pressure 15-2400 psi and high temperature (24-800 °C) can be accurately measured simultaneously [10].

In addition to passive sensing applications, regenerated gratings can offer considerable potential for applications in high-power laser [4] and active fiber sensing areas, where internal temperatures of fiber lasers can anneal conventional gratings out under high laser output power. With specially optimized optical fibers and strong seeds, regenerated gratings with 98.5% reflectance (~18 dB) can be readily fabricated [11], which is normally sufficient for laser oscillation with a relatively small cavity size.

In this report, we present studies and characterization of high-temperature stable distributed Bragg reflector (DBR) fiber lasers using the regenerative grating technique. Two regenerated gratings are used as reflectors in a DBR fiber laser for high-temperature operation. The laser performance was characterized from the room temperature to 750°C. Continuous monitoring for the laser output power was performed to quantify its stability at elevated temperatures. The regenerated gratings and output power of the laser are shown to be stable at 750 °C for more than 7 hours. For fiber lasers demanding high-temperature stability or high-power operation, regenerated grating based DBR fiber laser (RDBR) stands out as a simple and reliable solution.

In this work seed gratings were fabricated in standard telecommunications fibers (Corning SMF-28). To enhance photosensitivity, the fibers were soaked in a hydrogen chamber at $T \sim 25$ °C, $P \sim 2400$ psi (165 bars) for about 1 week. Two $L = 2.5$ cm long FBGs with $\lambda_{Bragg} \sim 1550$ nm were inscribed into the fiber core using a 248 nm KrF laser and a phase mask. A cumulative fluence of $f_{cum} = 1.32$ kJ/cm^2 was used to produce highly saturated gratings with pulse fluence $f_{pulse} \sim 50$ mJ/cm^2 and laser repetition rate 20 Hz. The spectra of two seed gratings with matched resonant wavelengths are shown in **Fig. 41**. Excessive UV exposures induced $\Delta n_{DC} > 10^{-3}$ index change in the fiber core and index modulations were estimated to be $\Delta n_1 = 0.0015$ and $\Delta n_2 = 0.0013$ for the two gratings FBG1 and FBG2 respectively shown in **Fig. 41**.

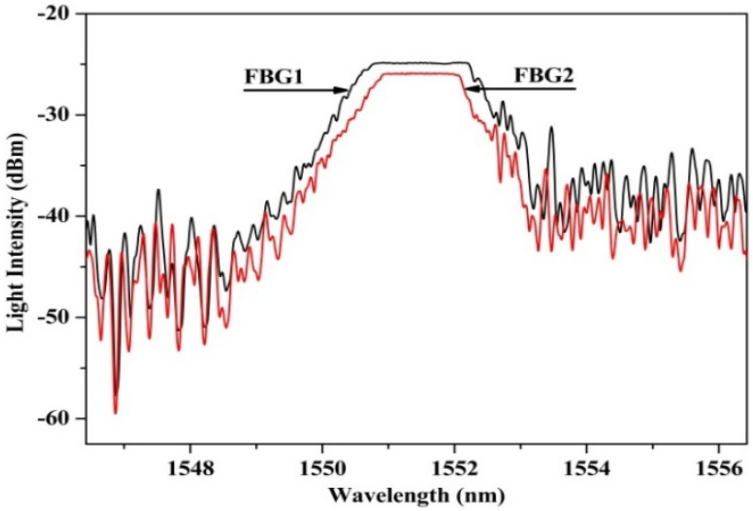

Fig. 41: Reflection spectra of the two matched fiber Bragg gratings.

Two matched gratings were fusion spliced to both ends of a 15 cm long erbium doped fiber with absorption of 57.0 dB/m at 980 nm (ER110-4/125 by nLight). The FBG2 in **Fig. 41** with relatively weaker index modulation was used as the output coupler for the laser cavity. The spliced fiber was then post-hydrogen-loaded [8] in the hydrogen chamber for t = ~ 2 days before the regeneration process. After being removed from the hydrogen chamber, the fiber laser was immediately taken to a box furnace for thermal treatment. The temperature of the furnace was isochronally raised up to T = 800 °C in t ~ 2.5 hr. Seed gratings were then annealed at T = 800 °C for t > 50 hr. The evolution of the grating spectrum is shown in **Fig. 42**, and the changes for λ_{Bragg} and reflection are shown in **Fig. 43**. It is worth noting that the regeneration process of the two gratings was measured together. Thus both of the gratings contributed to the reflection and the curve of peak wavelength shown in **Fig. 43**. There are five steps involved in the regeneration process. During Step A labeled in **Fig. 43**, the temperature of the box furnace isochronally increased at the rate of 5 °C/min. A slow growth in reflection was initially observed. This is mainly due to the degraded absorption of erbium doped fiber [12]. When the fiber temperature was raised to T = 800 °C, the isothermal annealing started. The erasure of the seed gratings occurred during this period (labeled as Step B). This was followed by grating regeneration labeled as Step C. The strength of the regenerated gratings increased steadily during this period. A blue shift in λ_{Bragg} was also observed in Step B and C, which is attributed to relaxation of UV-induced Δn_{DC}. At the early stage of the regeneration, two reflection peaks were on site as shown in **Fig. 42**. It is probably derived from the slightly different regeneration paces of FBG1 and FBG2, respectively. Peak reflectivity of regenerated FBGs increased and became stabilized after t ~ 32 hr. The double-peak features disappeared once both FBGs were stabilized. In the last step, the regenerated FBGs were allowed to stabilize for another 5 hours till the FBG wavelength fluctuation was below the minimal resolution of the optical spectrum analyzer (OSA, Agilent 86140B with 70 pm resolution) and the fluctuation of FBG strength was also less than 0.01 dB/hr at T = 800 °C. The index modulation of the regenerated grating FBG2 in **Fig. 41** was estimated to be $\Delta n_{reg} = 0.36\times10^{-4}$, resulting in more than 10 dB rejection in transmission with a FWHM bandwidth of 130 pm.

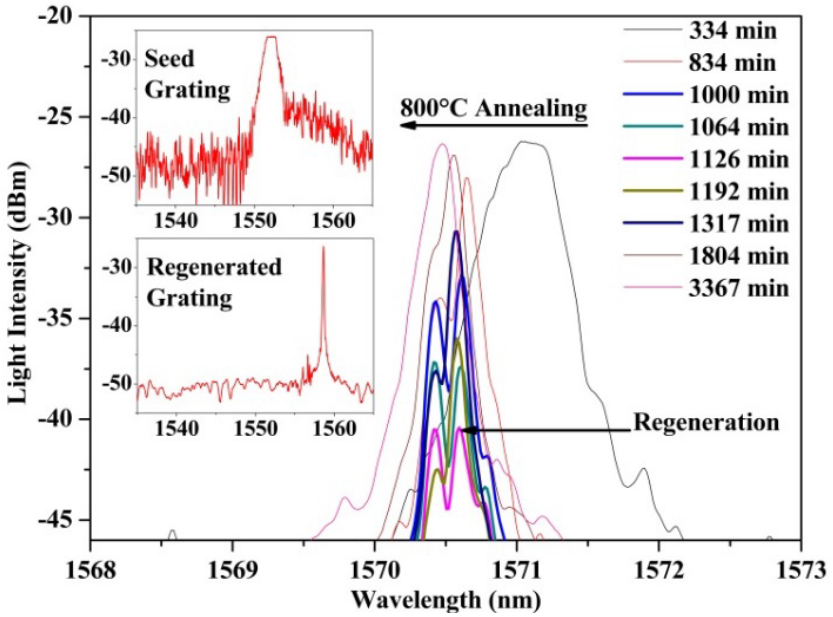

Fig. 42: Evolution of grating reflection spectra. Insets, reflection spectra of the seed at room temperature (T = 26 °C) and regenerated grating at 800 °C.

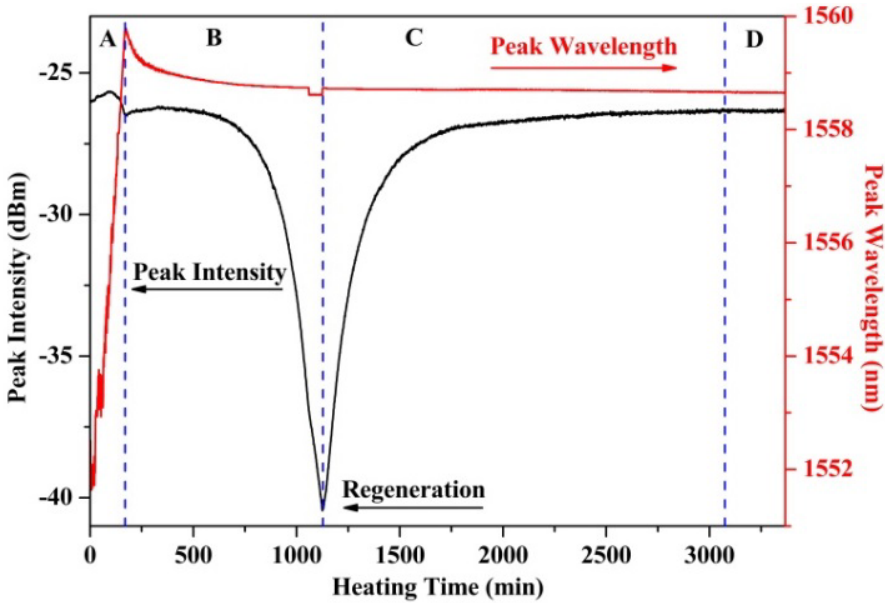

Fig. 43: Changes of grating strength and resonate wavelength during the regeneration process.

After the thermal regeneration process, the lasing characterization of the fiber laser was performed in a box furnace. A 980 nm diode laser, a wavelength division multiplexer, and the OSA were used for optical pumping and measurements respectively. The laser performance was characterized between room temperature (T = 26 °C) and 750 °C, which is 50 °C below the regeneration temperature. **Fig. 44** presents lasing wavelength dependence on temperatures. Two

linear wavelength-temperature coefficients are obtained in respective temperature regimes. In low temperature range from 26 – 300 °C, λ_{Bragg} shifted linearly as a function of temperature where $\partial\lambda/\partial T \sim 0.0132$ nm/°C. Above 300 °C in high temperature range, the coefficient increases to $\partial\lambda/\partial T \sim 0.0142$ nm/°C. This changing temperature dependence in low and high temperature regimes is very similar to that of regenerated gratings [9].

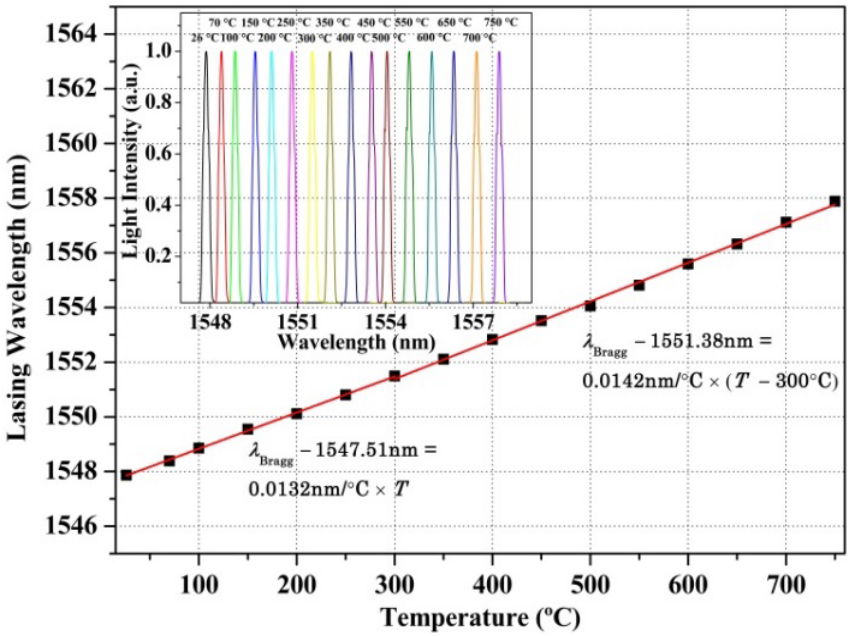

Fig. 44: Thermal wavelength shift of the fiber laser output (square) and its piecewise linear fitting curves (red). Inset, the normalized laser spectra under different temperatures.

The laser performance was further studied by quantifying the slope efficiency under different temperatures. Measurements of laser output versus pump power curves are shown in **Fig. 45**. At room temperature T = 26 °C, the laser exhibits the slope efficiency of η_s = 0.46%. When the temperature was raised to T = 500 °C, the efficiency decreased to η_s = 0.175%, due to the degraded gain spectrum, where the gain is depleted with increasing temperature by changing the saturated population inversion [12]. At the highest temperature T = 750 °C, the laser efficiency was significantly reduced to η_s = 0.069%. The lasing threshold also increases due to the gain degradation at high temperatures. The threshold increased from P_{th} = 20 mW at the room temperature T = 26 °C to P_{th} = 27 mW at T = 500 °C and finally P_{th} = 34 mW at T = 750 °C. Despite the gain degradation, the output power of the laser can reach P_{out} > 1mW at all test temperatures.

To study high-temperature performance and stability of the fiber laser, several heating and cooling cycles between 26 and 750 °C were carried out for a period over 120 hr. No decay was observed in the grating strength or the lasing characteristics. **Fig. 46** shows the stability characteristics of the laser output power during a period of 7 hour's isothermal heating at T = 750 °C. The optical pump for the fiber laser was set at P_{pump} = 67 mW. The OSA was used to measure the fiber laser output every minute. The total output power fluctuation shown in **Fig. 46** is 1.06% with a 60-μW output power.

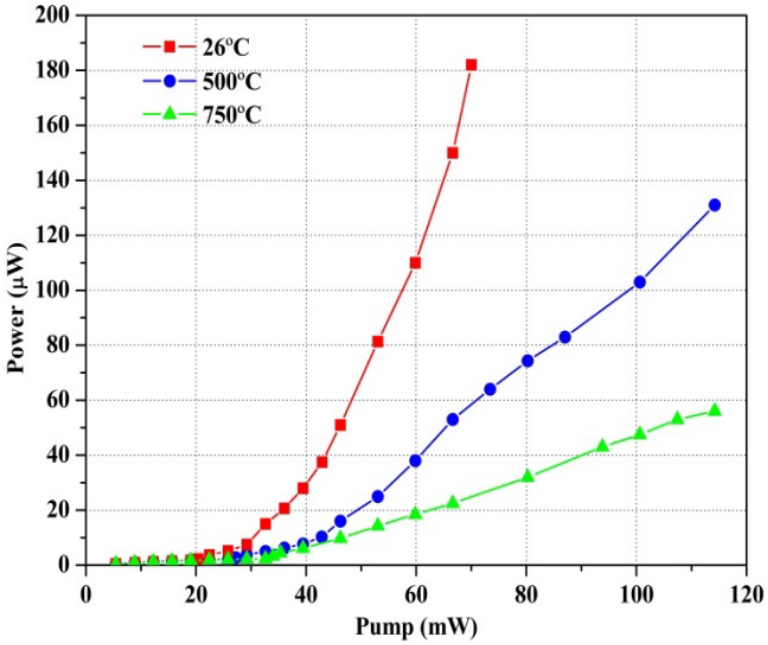

Fig. 45: Fiber laser output versus 980 nm pump power at three different temperatures.

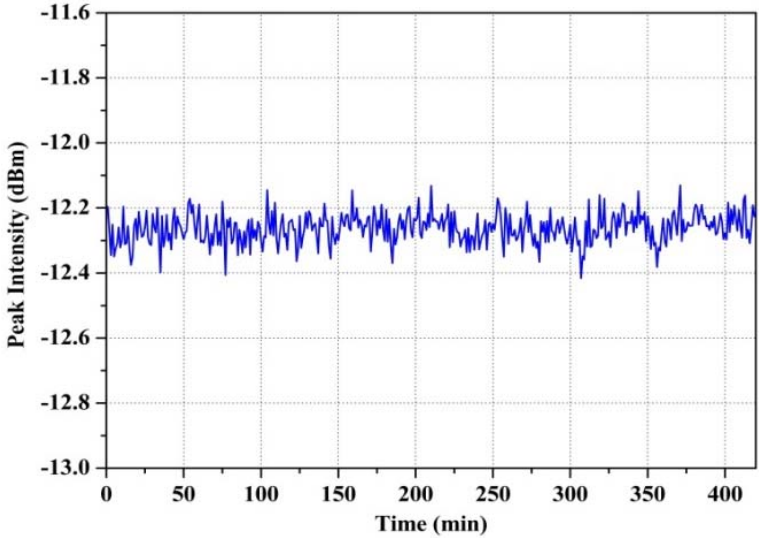

Fig. 46: Measured fiber laser output power over 7 h at 750 °C.

In summary, we have applied the thermal regeneration process, a low-cost fiber Bragg grating fabrication technique, to produce an erbium-doped DBR (or RDBR) fiber laser for high-temperature environment operation up to 750 °C. Despite a long fiber laser cavity, the RDBR fiber laser maintained stable operation at 750 °C for over 7 hours with no performance degradation observed. The index modulation of the regenerated grating observed in this work might also be sufficient to produce distributed feedback laser with much better longitudinal mode stability. The thermal regeneration FBG fabrication process opens new possibilities to design and implement fiber laser sensors for extreme environments.

7. Fiber-optic flow sensors for high-temperature-environment operation up to 800°C

During this performance period, we have taken the regenerative grating concept even further. This led to a new fiber optic flow sensors rated for a record-high operation temperature at 800°C. This work has been published on Optics Letters, we include results in this report.

Gas flow measurement plays important roles in various industrial sectors. It provides vital information for a large number of applications such as process controls, fossil-fuel and nuclear electric power generation, transportation, environment monitoring and etc. To perform flow measurements, a large number of flow sensors based on various mechanical, electronic, and micro-electro-mechanical system (MEMS) structures [1] have been developed. These sensors can perform effective flow measurements at the room temperature or slightly elevated temperatures (e.g. < 200 °C). However, a number of industrial and aerospace applications demand flow sensors with much higher operational temperatures (> 500 °C). These are not attainable by current state of the arts such as MEMS technology. To address this technical challenge, this work presents a low-cost and compact all-optical-fiber flow sensing technique that can provide rapid and accurate gas flow measurements from the room temperature to 800 °C. This is, to our best knowledge, the highest operational temperature for a flow sensor.

Fiber-optic sensors are well-known for their resilience in many harsh conditions including in high-temperature, corrosive, and strong electromagnetic environments. Over the last decade, various optical-fiber-based flow sensors have been reported, largely based on two schemes: fiber optical interferometry [2, 3] and optical hot-wire anemometry (Optical HWA). Among different designs of optical flow sensors, the HWA is one of the most widely adopted flow measurement techniques, thanks to its simplicity and reliability. HWA-based flow sensors determine flow rate by measuring heat transfer between a heated element and adjacent temperature sensors [4].

Compared with electrically heated HWA flow sensors, fiber-optic sensors can also be heated optically to perform flow measurements. Using various optical coupling schemes [5-11], in-fiber light has been used to heat up a section of fiber containing a sensing element (e.g. a fiber Bragg grating or FBG) to perform temperature measurements. The optical HWA can be more resilient than those using the electric heating for high-temperature applications. This is because the optical fiber, as a power delivery cable, can sustain much higher temperatures than metal wires.

In this work, we demonstrate an all-fiber high-temperature flow sensor using the optical HWA rated for 800 °C operation. The sensor consists of an in-fiber optical heating element using high-attenuation fibers (HAFs). High-temperature-stable regenerated FBGs (RFBG) [12-14] were induced in HAFs and standard telecom fibers (SMF-28) as temperature sensors to gauge flow-induced heat transfers. The schematic of the experiment setup is shown in Fig. 47. A high-power erbium doped fiber amplifier (EDFA) was built to provide up to 700-mW optical power to heat the HAF via a circulator. A RFBG in HAF was used to measure the temperature of the optical heating elements. Another RFBG formed in SMF-28 located at upper stream of the gas flow was used to measure the ambient temperature surrounding the heating element.

The wavelengths of FBG sensors were monitored by an optical spectrum analyzer (OSA, Agilent 86140B with 70 pm resolution). A tube furnace was used to provide high-temperature environments for sensor testing. During measurements, the fiber sensor was inserted in a quartz tube (OD: 6 mm, ID: 4 mm). At the input side, N_2 gas was introduced through a tee tube fitting. The fiber was sealed using a

rubber ferrule. At the exit of the flow tube, the fiber was placed on a tapered v-groove fiber holder (Thorlab HFV002) to ensure that no contact between the fiber and inner wall of the tube was made. A

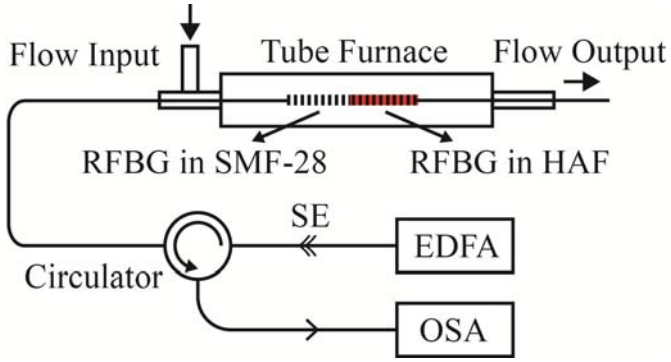

Fig. 47. Schematic of the experiment setup for sensor calibration and characterization.

calibrated mass flow controller regulated the input flow rate of N_2 gas. The sensor was tested under flow rates from 50 cubic centimeters (CCM) to 500 CCM, corresponding to mean flow velocity at the entry of the quartz tube ranging from 0.066 m/s to 0.66 m/s. At this velocity range, the gas flow inside the quartz tube is considered as laminar only [15].

Unlike conventional Type I FBGs which normally degrade rapidly at temperatures, RFBGs can be stable at the same temperature where it is regenerated (800 °C to 1295 °C [14]). This technique provides a low-cost approach to fabricate various sensors capable of high-temperature operations. To fabricate the fiber sensor based on regenerated gratings, two L = 1 cm long seed FBGs with λ_{Bragg} ~ 1543.55 nm and λ_{Bragg} ~ 1546.75 nm were inscribed in SMF-28 and HAF (CoreActive, attenuation coefficient 1 dB/cm) respectively. To enhance their photosensitivity, both optical fibers were soaked in a hydrogen chamber at T ~ 25 °C, P ~ 2400 psi (165 bars) for about 1 week before the laser inscription. A 248-nm KrF excimer laser with pulse fluence f_{pulse} ~ 50 mJ/cm^2 and repetition rate RR = 20 Hz was used to inscribe the FBGs. A cumulative fluence of f_{cum} = 0.09 kJ/cm^2 was assigned to produce the FBG in SMF-28 while f_{cum} = 1.2 kJ/cm^2 was applied to HAF. These lead to the FBG spectra shown in the left inset of Fig. 48. After the inscription, the samples were annealed at 120 °C for t ~ 12 hours. These two FBGs were then fusion spliced together to form the optical flow sensor as demonstrated as well in Fig. 47.

The regeneration process starts from a post-hydrogenation process [16]. Fiber sensor samples were first put back into the hydrogen chamber for post-hydrogen-loading at 2400 psi to enhance its photosensitivity. This is a key process for successful regeneration, especially for FBGs in HAFs. The post-hydrogen-loading lasted for t = 1 week. Then the fiber sample was placed in a box furnace for the thermal regeneration. A typical regeneration process is shown in Fig. 2. The temperature of the furnace was isochronally increased to 850 °C with a rate of 5 °C/min in step A and then held steady in both step B and C for isothermal annealing. FBGs in both SMF-28 and HAF were annealed rapidly as the temperature rose (step A), however, with different decay patterns. This is probably due to double-cladding fiber structures in HAF. During the grating erasure, the onset of a blue shift in λ_{Bragg} is attributed to the thermal relaxation of UV-induced average refraction index change Δn_{DC}. The full erasure of both FBGs occurred at the end of step B, which lasted t ~ 250 min. This was followed by their subsequent grating regeneration in step C. Fig. 2 shows that the FBG in SMF-28 was regenerated much faster than that in HAF. When both RFBGs approached their steady states after t ~ 870 min of the thermal annealing at T = 850 °C, the furnace temperature was elevated to 1000 °C for RFBG stabilization with the same rate

of 5 °C/min as shown in step D. Both FBGs were finally stabilized after $t \sim$ 580 min of isothermal annealing at 1000 °C.

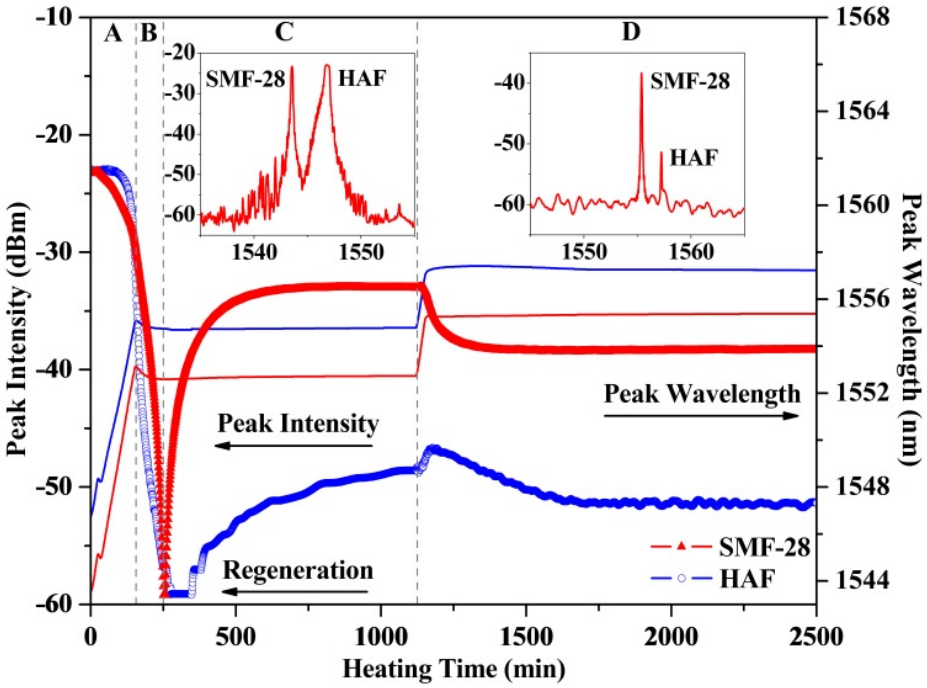

Fig. 48: Changes of grating strengths and resonant wavelengths during the regeneration process for FBG in SMF-28 (red) and HAF (blue) respectively. The dot traces are for FBG peak intensity while line traces are for FBG wavelength. Insets, reflection spectra of the seeds at room temperature (T = 25 °C) and regenerated gratings at 1000 °C.

Once FBGs were regenerated, the flow sensor was characterized using the experiment setup shown in Fig. 47. The thermal responses of the two gratings were first measured and presented in Fig. 3. RFBGs in both HAF and SMF-28 exhibit slightly different thermo-optic coefficients for temperature from the room temperature to 300 °C and from 300 °C to 800 °C [17] where piecewise linear regression was used to evaluate the wavelength-temperature coefficients $d\lambda/dT$ of FBGs in two temperature ranges as shown in Fig. 49. The wavelength-temperature coefficients determined in Fig. 49 are important to gauge optical heating performance of HAFs.

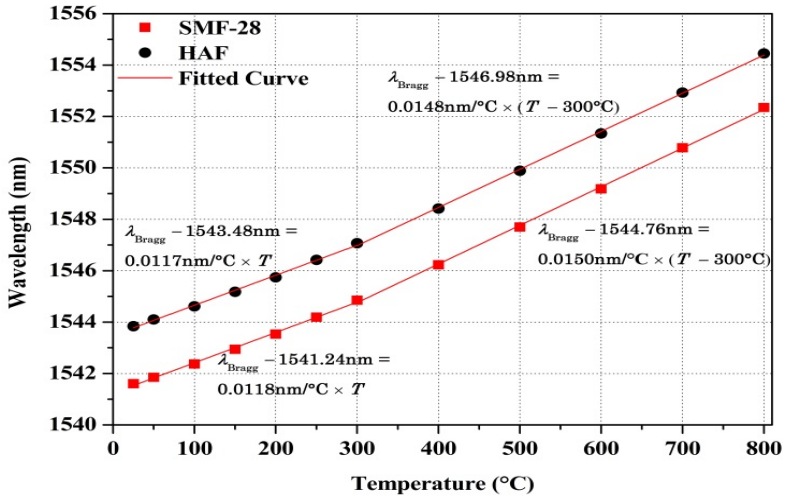

Fig. 49: Resonant wavelength versus ambient temperature for both RFBGs

The optical heating of the HAF sensor under different ambient temperatures was quantified by injecting optical power from the EDFA from 0 to 700 mW. Not all optical power was absorbed by the HAF. It was estimated that the optical power absorbed by the 1-cm HAF was 14 mW/mm with 700-mW input power. The optical heating performance of the HAF from the room temperature to 800 °C is presented in Fig. 50. The largest shift of resonant wavelength for the RFBG in HAF is equal to $\Delta\lambda = 2.31$ nm, corresponding to $\Delta T = 197.44$ °C at the room temperature. As ambient temperature increases, the optical heating becomes less efficient. At 800 °C the shift of resonant wavelength was reduced to $\Delta\lambda = 1.09$ nm using 700-mW optical power, corresponding to $\Delta T = 73.65$ °C.

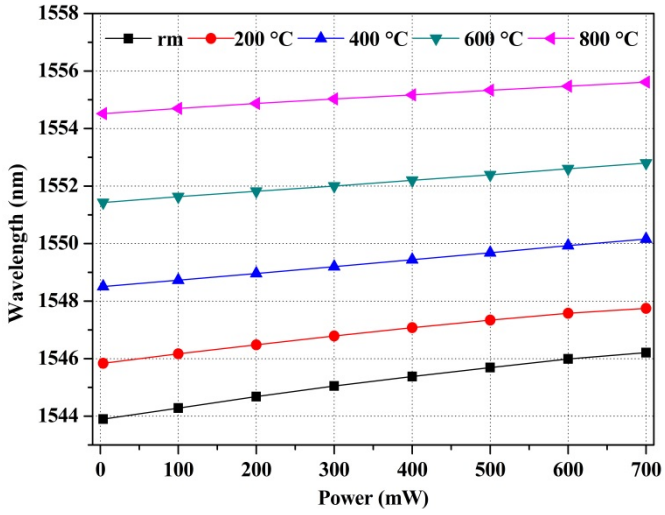

Fig. 50: Heating performance of the HAF under different ambient temperatures.

The operations of the flow sensor at the room temperature and at 800 °C are shown in Fig. 51. Reflection spectra for RFBGs in SMF-28 and HAF in ambient temperatures are shown in black traces. When the HAF section of the fiber absorbed optical power of 14 mW/mm at the room temperature (Fig.

5a), the RFBG wavelength in the HAF shifted for $\Delta\lambda_3 = 2.31$ nm ($\Delta T = 197.44$ °C). The upper stream RFBG in SMF-28 also experienced a small red shift in resonant wavelength for $\Delta\lambda_1 = 0.13$ nm, equivalent to temperature rise $\Delta T \sim 11$ °C as shown in Fig. 51a, which was largely due to the thermal conduction between two grating areas. The temperature of this upper stream RFBG sensor would be used as the reference to gauge the ambient temperature surrounding the heated element (HAF). Thereafter, the flow of N_2 was applied with a rate of 500 CCM (0.66 m/s), where convection cooling becomes the major factor responsible for heat loss of the HAF. The resonant wavelength of the upper stream RFBG in SMF-28 shifted back toward its original by $\Delta\lambda_2 = -0.15$ nm, lowering the surface temperature of the sensor to $T = 23.31$ °C which was nearly 2 °C lower than the preset ambient temperature $T = 25$ °C, probably due to the temperature drop of decompressed N_2 itself. Meanwhile, the RFBG of HAF incurred a great blue shift in resonant wavelength for $\Delta\lambda_4 = -0.71$ nm, corresponding to a temperature drop for $\Delta T = 60.68$ °C.

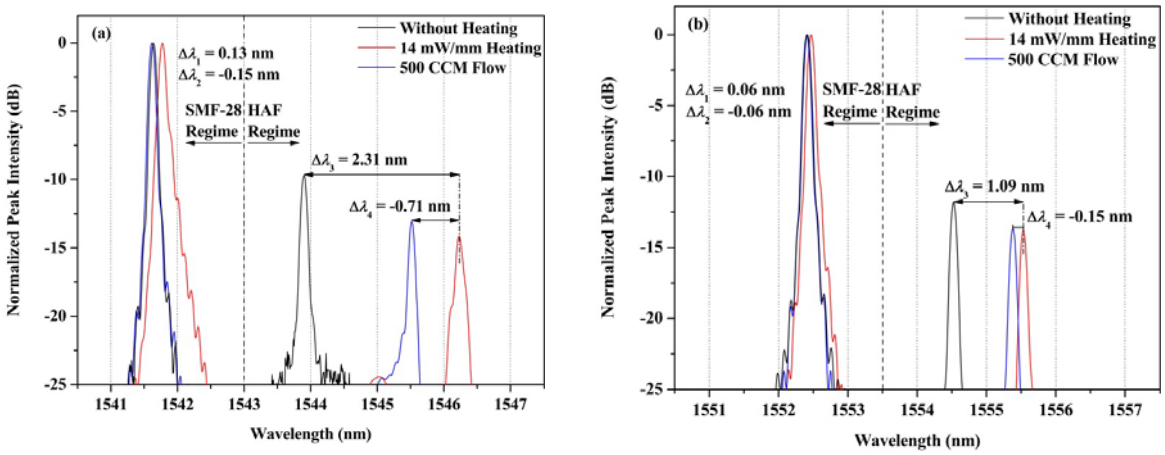

Fig. 51: Reflection spectra of both RFBGs in SMF-28 and HAF under different heating, flow conditions and ambient temperatures: (a) 25 °C; (b) 800 °C.

At $T = 800$ °C, the absorption of 14 mW/mm optical power produced smaller wavelength shifts for both the reference RFBG ($\Delta\lambda_1 = 0.06$ nm) and the RFBG in HAF ($\Delta\lambda_3 = 1.09$ nm) as shown in Fig. 51b. The introduction of 500-CCM N_2 gas flow shifted the wavelength of the reference RFBG back to its original position ($\Delta\lambda_2 = -0.06$ nm). A blue shift $\Delta\lambda_4 = -0.15$ nm of the RFBG wavelength in HAF was observed, corresponding to a temperature drop $\Delta T = -10.14$ °C of the optically heated HAF. The temperature drops measured by the RFBG in HAF and the reference temperature measured by the RFBG in SMF-28 can be combined to gauge the flow rate of N_2.

For a HWA flow sensor, the temperature change from the heating element due to the gas flow can be related to the flow velocity v by [4],

$$H_{power} = \Delta T_h (A + B\sqrt{v}) \quad (1)$$

where H_{power} is the power absorbed by the heating element, ΔT_h is the temperature change from the ambient background on the HWA induced by an isothermal flow field, A and B are empirical coefficients. In our case, ΔT_h is determined by the temperature changes on the heated RFBG in HAF and the ambient temperature measured by the reference RFBG in SMF-28 located at the upper stream of the gas flow according to,

$$\Delta T_h = \left(\frac{d\lambda}{dT}\right)^{-1}_{HAF}(\Delta\lambda_3 + \Delta\lambda_4) + \left(\frac{d\lambda}{dT}\right)^{-1}_{SMF-28}(\Delta\lambda_1 + \Delta\lambda_2) \quad (2)$$

where $(d\lambda/dT)_{HAF}$ and $(d\lambda/dT)_{SMF\text{-}28}$ are the wavelength-temperature coefficients of RFBGs in both HAF and SMF-28 fibers, which are determined by Fig. 49. The accurate measurement of the ambient temperature by the reference RFBG is critical to ensure accurate flow measurements. This is because that the introduction of gas flow can alter the ambient temperature in the vicinity of the HWA sensors [18].

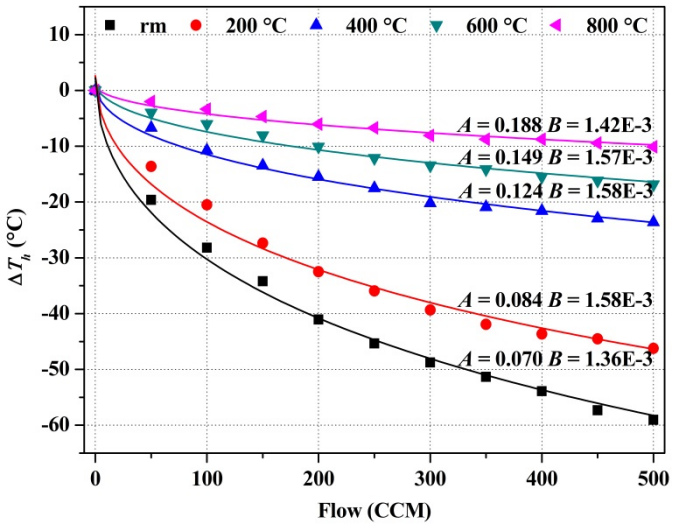

Fig. 52: Calibrated sensor responses of the flow under different ambient temperatures shown with fitted curves based on the HWA theory. A and B are coefficients of the fitting function with units of mW/mm/°C and mW/mm/°C/(m/s)$^{1/2}$ respectively.

The performance of the flow sensor under the maximum optical heating power (14 mW/mm) was quantified and shown in Fig. 52 with fitted curves derived from (1). The empirical coefficients A and B of every fitted curve are also included in the figure. The fitted curves match well with the experimental flow measurements at all temperatures. This indicates effective operation of the all-fiber hot-wire flow sensor operating under both the room temperature and at elevated temperatures. Due to the nature of HWA, the sensitivity of the sensor reduces at high temperatures due to lower heating efficiencies of the HAF. However, this problem can be remedied by increased optical heating power or using HAF with higher attenuation coefficients.

In conclusion, this work presents an all-optical high-temperature flow sensor based on hot-wire anemometry. Using in-fiber light as both the heating power and the interrogation light source, a pair of high-temperature-stable RFBGs were used to gauge the heat transfer from an optically powered heating element (HAF) induced by the gas flow. The entire flow sensor was constructed in one silica fiber and interrogated/powered through one fiber feed through. Reliable gas flow measurements were demonstrated for a wide temperature range from the room temperature to 800 °C. The fiber sensor technique presented in this paper provides a low-cost and reliable solution for flow sensing for high-temperature harsh environments.

8. SCALABLE MANUFACTURING OF METAL OXIDE NANOMATERIALS

Based upon our earlier work on metal oxide fiber optical sensor (pg. 32-38 of this report), we further expand the development of metal oxide nanomaterials for sensing. SnO2 metal material developed earlier is not suitable for high-temperature application. Therefore, we applied similar nano-engineering scheme to produce functional nanomaterials for high temperature chemical sensing. These works focus on ZnO and TiO_2 and their doping variants. This final section of reports will detail the process of nano-material synthesis and applications for on-fiber applications.

To engineer refractive index or dielectric permittivity of metal oxides using nano-engineering scheme is a relatively old idea. Based on Maxwell-Garnet effective medium theory, the modification of dielectric permittivity requires that the geometrical features of nanostructures are much smaller than the wavelength of the light. Recent advance in nanomaterial synthesis has provided effective techniques to structure metal oxide materials in three dimensions at the sub-wavelength (< 20 nm) scales. In this paper, block copolymers templating is used to control porosity of metal oxide at 20 nm length scale to control refractive index.

Block copolymers are an interesting type of polymers widely used for nanostructure synthesis [14]. A rich group of nanostructures can be obtained by templating with block copolymers, where in most cases polymers form interconnected structures, and functional materials infiltrate voids. From the available block copolymers Pluronic F-127, a triblock copolymer, was chosen since it has higher temperature stability and it is known to form 3D interconnected structures in most cases [15]. Block-copolymer template combined with sol-gel solution processing approach allows the synthesis of nanoporous structured thin film of metal oxides or silica [15]. The polymer template will be removed after pre-heat treatment and the crystalline nanoporous structure will be directly developed around the template. The porosity of the film can be tuned by controlling the mole fraction of the copolymer with respect to the metal source, which will allow us to tune the effective index of the film.

In this work, metal chlorides or alkoxides were used as the precursor of the sol-gel solution in our experiment. HCl was used as a stabilizer. Pluronic F-127 was used as the structure template. First, a certain amount of HCl (37%) and ethanol were mixed together with precursor. And different amount of Pluronic F-127 was added into the solution to obtain different porosity. Then the solution was stirring for 1 hour at 60 ^{o}C on the hot plate to obtain a homogeneous solution. Afterwards the solution was cooled to room temperature and aged for 24 hours. The whole process can also be performed in the presence of dopants, such as Pd. The thin films were produced by spin coating the solutions on silicon wafer in order to characterize the refractive index of nanoporous SiO_2 and TiO_2 with different porosity. Each solution was spin-coated at 2500 rpm for 30 seconds on silicon wafer. The freshly coated wafers were placed in an oven and preheated to 60 °C, followed by a heating treatment at 130 °C for 1 hour. Then the temperature slowly increased (1 °C/minute) to 600 °C and held there for 1 hour. Afterwards, the samples were cooled to room temperature at 3 °C/minute. Transmission electron microscopy (TEM) was used to observe the structure of synthesized thin film, and spectroscopic ellipsometer was used to measure the refractive index and the porosity of the film.

To develop metal oxide sensitive to hydrogen, Pd dopants were incorporated into the TiO_2. The Pd-doped TiO_2 for sensor use was synthesized using the alkoxide route of sol-gel method. Titanium isopropoxide ($Ti(OCH(CH_3)_2)_4$) was used as precursor. Palladium chloride ($PdCl_2$) was utilized as dopant. The molar ratio of Pd and Ti was 0.03. Room-temperature 0.5 g ($Ti(OCH(CH_3)_2)_4$) was added into a mixture of 2.5 g ethanol and 0.25 g HCl during stirring. Pd solution was prepared by adding 0.02 g $PdCl_2$ (corresponding to 3 at.% of Ti atoms) into 1.85 g ethanol, and 0.15 g HCl was added to enhance the solubility of $PdCl_2$. The mixture was stirred 3 hours to completely dissolve the $PdCl_2$. Then two solutions were mixed together with 0.5 g Pluronic F-127, followed by stirring for 12 hours at 60 ^{o}C. Then the solution was cooled to room temperature and aged for 24 hours and ready for coating.

Figure 53(a) presents a TEM image of refractive index controlled TiO_2. The interconnected 3D structure with features about 20 nm regime, which are formed by the use of block copolymer Pluronic F-127, is clearly visible. The pores keep almost circular shape and are distributed uniformly. According to effective medium theory, the refractive index of a material can be lowered by introduction of no scattering porosity [16]. This deep sub-wavelength feature formed by block copolymers template combined with the solution processing provides a way to tailor the index of the SiO_2 and TiO_2 as we expect. Figure 53(b) and (c) summarize refractive indices of nano-porous TiO_2 and SiO_2 coated on silicon wafer with different porosity. The refractive indices were obtained by a Jobin-Yvon UVISEL spectroscopic ellipsometer. The measurement data were fit using minimization algorithms. Results presented in Figure 53(b)-(c) show that the index of SiO_2 and TiO_2 can be modified in a large range as desired. The refractive indices of the nanoporous SiO_2 can be modified down to about n~1.2 at 800 nm. For nano-porous TiO_2 film, the measured refractive index can be much lower than fully dense TiO_2 and the index can be modified to compatible with silica based optical components. At 1550 nm, the index of TiO_2 with porosity 50% is about 1.43. This value is slightly lower than the D-shaped fiber intrinsic core index of 1.46, which will ensure that the light will be confined in the core of the fiber and minimize the unwanted transmission loss after coating.

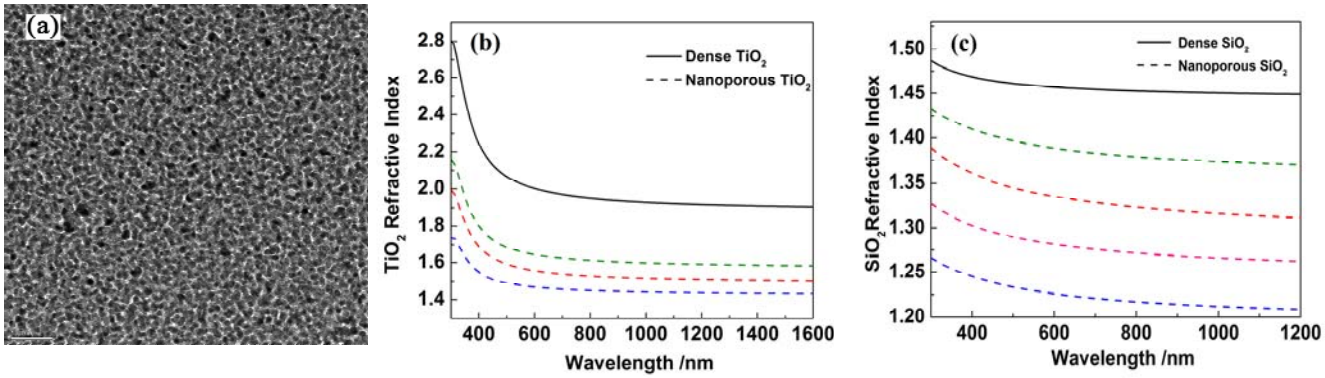

Fig. 53: (a) TEM picture of the TiO_2 film synthesized by using block-copolymer template combined with sol-gel solution processing; Refractive indices of the (b) nanoporous TiO_2 and (c) nanoporous SiO_2 film with different porosity.

INTEGRATION OF METAL OXIDE ON FIBER FOR HYDROGEN SENSING

Metal oxides have been widely used in conductometric type electronic sensors, or chemiresistors, it is well known that changes in the conductive properties are to be expected. Specific doping by certain metals, such as Al, Pd, and Pt [17,18], are known to modify the free electron concentration and mobility of metal oxides, which can enhance their sensitivity, selectivity and response times. However, these electronic sensors cannot function in harsh environments such as extremely high temperatures (e.g. < 500^{o}C). In this paper, we demonstrate a fiber-optic sensing technique using metal oxide nanomaterials to perform hydrogen measurements at extremely high temperatures up to 700^{o}C, which cannot be attained using electronic sensors.

Hydrogen has been the focus of a great amount of attention recently as a clean and environmentally friendly energy source. However, the dangers associated with the use and storage of hydrogen have always been a tremendous problem due to the wide explosive range (4-75%) and small ignition energy (0.02mJ). Security systems monitoring of the concentration of hydrogen gas demand fast, sensitive and reliable hydrogen sensors, especially for large-scale energy generation systems where a large amount of hydrogen is stored and consumed at high temperatures. Semiconductor metal oxides such as SnO_2, TiO_2, and ZnO are widely used for hydrogen gas sensing applications due to their electrical conductivity

changes after adsorption of hydrogen gas [18-22]. Despite of the intrinsic properties of the material, the sensitivity to gases is also related to the structure of the sensing material, especially on the porosity and grain size. Nanostructured material is believed to be more sensitive to chemicals due to the increased surface-to-volume ratios and reduced cross sections [23]. Compared to other metal oxides, TiO_2 is well known for its wide band gap and structural stability at high temperatures. Doping of TiO_2 has been theoretically and experimentally confirmed as a feasible way to obtain tunable semiconducting properties, which leads to the change of sensitivity [24]. Palladium is a good catalyst in oxide semiconductor hydrogen sensors. For Pd-doped TiO_2, the Pd acts as catalyst to dissociate hydrogen molecules and supply atomic hydrogen to TiO_2.

Most of the semiconductor metal oxide hydrogen sensors are electrical sensors based on resistance measurement. All-optical fiber hydrogen sensors, due to their explosion-proof nature and immunity to electromagnetic interference, have been developed as well, such as fiber Bragg grating [25], surface plasmon resonance sensor [26] and evanescent sensor [27]. These sensors can perform effective hydrogen concentration measurements at slightly low temperature, usually lower than 400 ^{o}C. The sensitivity of these sensors will degrade with the increase of temperature due to thermal instability. However, there are amount of industrial application demand to monitor the hydrogen concentration above 600 ^{o}C. To address this problem, we develop this all-optical-fiber hydrogen sensor with Pd-doped TiO_2, which can provide rapid hydrogen concentration measurement up to 700 ^{o}C. With the nanostructure in sub-wavelength regime, the refractive index of Pd-doped nanoporous TiO_2 can be tailored to match the fiber core (n_{core} ~ 1.46) according to effective medium theory. A rapid and ultrasensitive high-temperature hydrogen senor was realized by using this Pd-doped nanoporous TiO_2 thin film coated D-shaped fiber, which is an optimally designed optical fiber sensor platform [23]. High-temperature-stabilized fiber Bragg grating is induced in D-shaped fiber for high-temperature resistance. The sensitivity of the sensor was investigated from 300 ^{o}C to 700 ^{o}C.

The D-shaped fiber used to prepare gratings was first soaked in pure hydrogen atmosphere at T ~ 25°C, P ~ 2400 psi for more than two weeks to enhance photosensitivity. Then, the strong grating with λ_{bragg} = 1551.5 nm was inscribed into the core of D-shaped fiber by using a 248 nm KrF laser and a phase mask. The spectra and schematic of the grating are shown in Figure 54. The grating was inscribed with strong reflection to survive high-temperature processing. In order to get a higher sensitivity, the residual 4 μm cladding material on the flat side of the D-shaped fiber was removed by placing it in a buffered HF solution (5 NH_4F : 1 HF) for 21minutes. After the etching process was finished, the etched grating was rinsed several times in deionized water and ethanol. Then the grating was dried for Pd-doped TiO_2 coating.

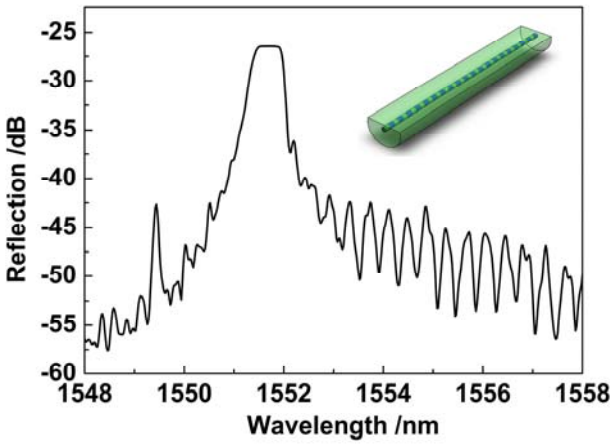

Fig. 54. Schematic of the Bragg grating inscribed on hydrogen loaded D-shaped fiber by UV light and the reflection spectrum of the seed grating.

The etched fiber with grating was immersed in the sol solution and coated through dip coating procedure at the speed of 0.2 mm/s. The coated fiber was dried in the air at room temperature overnight, and sol-gel Pd-doped TiO_2 film was formed by the hydrolysis. Then the coated fiber was put into a tube furnace and annealed with heating to 130 ^oC at 5 ^oC/min, and held there for 1 hour. Followed by heating to 600 ^oC at 3 ^oC/min and calcined for 1 hour. These procedures were conducted in air atmosphere. The FBG were stabilized at the same time. After these procedures, the coated fiber was cooled to 300 ^oC at 3 ^oC/min, and then switched from air gas to 5 vol. % H_2/N_2 for 1 hour with 40 ccm/min flow speed to reduce the PdO in the film. The schematic diagram of D-shaped fiber Bragg grating hydrogen sensor characterization system is shown in figure 55. The reflection spectrum of FBG sensor was monitored by an optical spectrum analyzer. A tube furnace that can control temperature up to 800 ^oC was used. The fiber was inserted in a quartz tube, which was placed in tube furnace. Two rubber ferules were used to seal both ends of the tube and to apply tension to ensure that the fiber has no contact to the inner wall of the tube. The sensor can be exposed to various concentrations of hydrogen balanced with nitrogen or pure nitrogen by using two calibrated mass flow controllers. Hydrogen concentrations from 0.25 vol. % H_2/N_2 to 5 vol. % H_2/N_2 were tested.

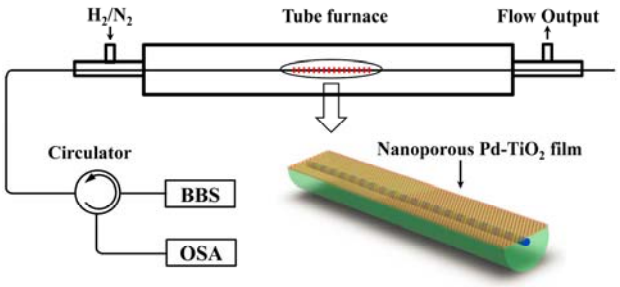

Fig. 55. Schematic diagram of Pd-TiO_2 nanoporous film coated on etched D-shaped FBG and hydrogen sensor characterization system.

The intensity of the Bragg resonance peak highly depends on the index of the coating. The light can barely transmit through the coated fiber before heating treatment due to the relatively high index of the uncalcined film cladding. The index of the coated film will decrease when Pluronic F-127 template and other organic solvent is removed by heating. In our experiment, the Bragg resonance peak disappeared after the coating and appeared again after temperature reached 300 ^oC. And the intensity increased via increasing temperature. Finally, the peak was stabilized at 600 ^oC with intensity around -60 dB. Figure 56(a) shows the hydrogen response of the sensor in ambient cycled from pure N_2 to 5% H_2 in N_2, and then back to pure N_2 at 600 ^oC. The intensity of the resonance peak decreased dramatically with exposure to H_2 and recovered back when N_2 ambient was restored. After the system was flushed with nitrogen gas, the results were repeated with a very small amount of baseline drift. This indicates the hydrogen sensor based on nano-porous Pd-TiO_2 coated etched D-shaped FBG is reliable at high temperature. Response time is an important sensitivity indicator of a sensor, which is defined as the time required for the sensor to reach its average lowest peak intensity. In order to measure the response time of the Pd-doped nano-porous TiO_2, the intensity of the transmission was directly measured. The response time of the sensor upon exposure to hydrogen is 7~8 s as figure 56(b) shows. The restore time of the sensor is about several minutes in pure N_2 flush. The restore time is believed to decrease dramatically if small amount of O_2 is added into the N_2.

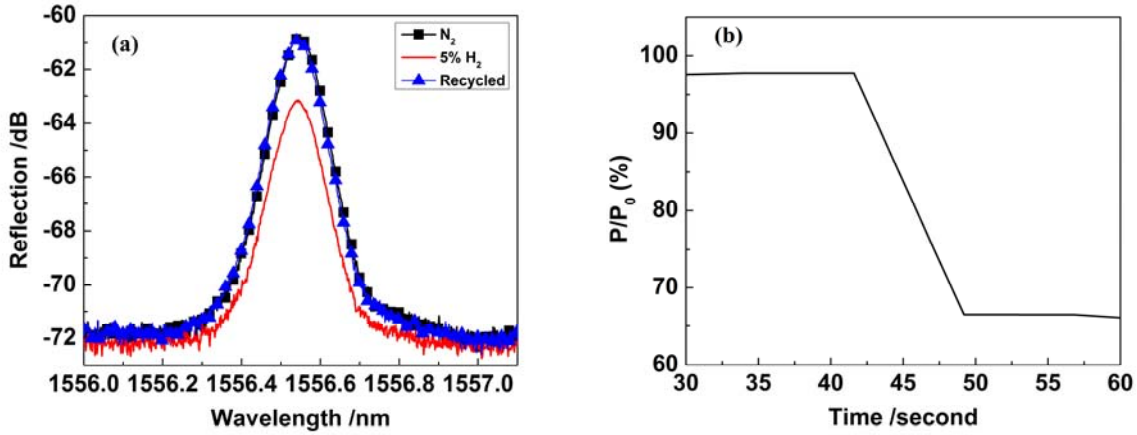

Fig. 56: (a) Spectra of the sensor cycled in 5% H_2 and N_2, (b) Response time of the hydrogen sensor.

Figure 57(a) presents the reflection spectra of the FBG exposed to H_2 with concentration range from 0.25% to 5% at the highest testing temperature of 700 ^oC. The reduction of 6-dB of FBG peak magnitude can be observed for the change of hydrogen concentration from 0% to 5%. The intensity of the peak has incurred more decrease compared with that at 600 ^oC, which indicates stronger optical absorption. The reduction of FBG peak is also accompanied by shift of FBG peak, which is the indication of refractive index change of FBG. An 80-pm FBG wavelength shift is noted in Figure 57(a). Given that up to 2% of guided light is propagated in Pd-doped TiO_2 coating, up to 4×10^{-3} of refractive index change could be due to the redox reaction of Pd-doped TiO_2 film. However, the FBG peak shifts could also be due to temperature variation. The thermal-optic coefficient of FBG in silica fiber is ~13 pm/^oC. The FBG wavelength shifts shown in Figure 57(a) could be attributed to up to 7 ^oC temperature fluctuation at the elevated temperature of 700 ^oC. Figure 57(b) shows the decrease of the peak intensity upon switching ambient from N_2 to 5 % H_2 as a function of temperature. The improvement of the sensor performance at high temperature is considered to be beneficial from more effective catalytic dissociation of H_2 in Pd-doped TiO_2 at higher temperatures. However, our experiments also show that the performance will degrade when temperature goes higher than 780 ^oC, due to thermal instability of the porosity structure at this temperature. Because the porosity structure begins to collapse when temperature is higher than 780 ^oC, which will decrease the surface to volume ratio and increase the refractive index of the film, resulting in large optic loss.

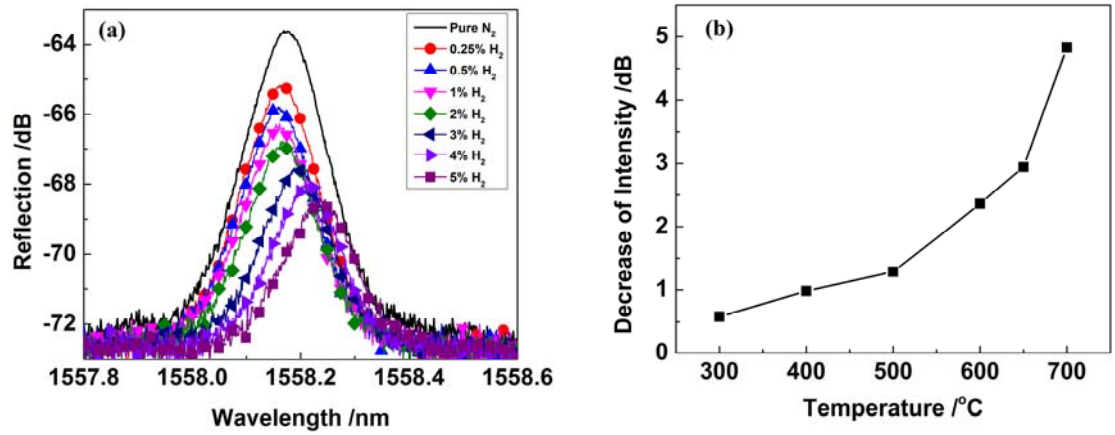

Fig. 57. (a) Spectrum of the coated D-shaped FBG exposed to 0.25%, 0.5%, 1%, 2%, 3%, 4%, 5% H_2 and pure N_2 respectively, (b) Peak intensity as a function of temperature for 5% H_2.

CONCLUSION

This project report presents a solution-based scalable nanofabrication scheme to manufacture metal oxides and their doping variants with controlled index of refraction. Through block copolymer templating, nanoporous Pd-doped TiO_2 3D nanostructure with pore size from 5 nm to 20 nm was synthesized. Through this approach, the indices of refraction of SiO_2 and TiO_2 can be controlled over a wide range from 1.2 to 2.4. In this paper, this new material synthesis technique has been successfully applied for new optical sensor developments. Using solution-based coating technique, Pd-doped TiO_2 functional coating were successfully integrated with high-temperature-stable fiber Bragg grating in D-shaped fiber for evanescent wave sensing for hydrogen at elevated temperatures up to 700^{o}C. Using the same nano-synthesis scheme, it is also possible to manufacturing other metal oxides with desired index such as SnO_2 and ZnO. Further, it is also possible to combine the solution-based processing scheme as demonstrated in this work, with other manufacturing schemes such as dip-pen nanolithography, dip coating, or ultrasonic spraying coating to produce metal oxide coating at large areas for scalable device fabrication at low costs.

Reference:

1. Y. Lai, A. Martinez, I. Khrushchev, and I. Bennion, "Distributed Bragg reflector fiber laser fabricated by femtosecond laser inscription," Opt. Lett. **31**, 1672-1674 (2006).
2. Y. Shen, Y. Qiu, B. Wu, W. Zhao, S. Chen, T. Sun, and K. T. V. Grattan, "Short cavity single frequency fiber laser for in-situ sensing applications over a wide temperature range," Opt. Express **15**, 363-370 (2007).
3. B.-O. Guan, Y. Zhang, H.-J. Wang, D. Chen, and H.-Y. Tam, "High-temperature-resistant distributed Braggreflector fiber laser written in Er/Ybco-doped fiber," Opt. Express **16**, 2958-2964 (2008).
4. N. Jovanovic, M. Åslund, A. Fuerbach, S. D. Jackson, G. D. Marshall, and M. J. Withford, "Narrow linewidth, 100 W cw Yb3+-doped silica fiber laser with a point-by-point Bragg grating inscribed directly into the active core," Opt. Lett. **32**, 2804-2806 (2007).
5. Z. Bowei and K. Mojtaba, "High-Temperature Resistance Fiber Bragg Grating Temperature Sensor Fabrication," Sensors Journal, IEEE **7**, 586-591 (2007).
6. S. Bandyopadhyay, J. Canning, M. Stevenson, and K. Cook, "Ultrahigh-temperature regenerated gratings in boron-codoped germanosilicate optical fiber using 193 nm," Opt. Lett. **33**, 1917-1919 (2008).
7. S. Bandyopadhyay, J. Canning, P. Biswas, M. Stevenson, and K. Dasgupta, "A study of regenerated gratings produced in germanosilicate fibers by high temperature annealing," Opt. Express **19**, 1198-1206 (2011).
8. E. Lindner, J. Canning, C. Chojetzki, S. Brückner, M. Becker, M. Rothhardt, and H. Bartelt, "Post-hydrogen-loaded draw tower fiber Bragg gratings and their thermal regeneration," Appl. Opt. **50**, 2519-2522 (2011).
9. T. Wang, L.-Y. Shao, J. Canning, and K. Cook, "Temperature and strain characterization of regenerated gratings," Opt. Lett. **38**, 247-249 (2013).
10. T. Chen, R. Chen, C. Jewart, B. Zhang, K. Cook, J. Canning, and K. P. Chen, "Regenerated gratings in air-hole microstructured fibers for high-temperature pressure sensing," Opt. Lett. **36**, 3542-3544 (2011).
11. J. Canning, M. Stevenson, J. Fenton, M. Aslund, and S. Bandyopadhyay, "Strong regenerated gratings," 750326-750326 (2009).
12. N. Kagi, A. Oyobe, and K. Nakamura, "Temperature dependence of the gain in erbium-doped fibers," Lightwave Technology, Journal of **9**, 261-265 (1991).
13. Z. Poole, P. Ohodnicki, R. Chen, Y. Lin, and K. Chen,: *Opt. Express*, 2014, vol. 22, pp. 2665-74.
14. M. C. Orilall, and U. Wiesner, : *Chem. Soc. Rev.*, 2011, vol. 40, pp.520-535.

15. S. Shao, M. Dimitrov, N. Guana and R. Kohn,: *Nanoscale*, 2010, vol. 2, pp. 2054-57.
16. B. E. Yoldas and D. P. Partlow,: *Thin Solid Films*, 1985, vol. 129, pp.1-14.
17. M. Zhang, Z. Yuan, J. Song, C. Zheng,: *Sens. Actuators, B*, 2010, vol.148, pp. 87-92.
18. J. Moon, J. A. Park, S. J. Lee, T. Zyung, and I. D. Kim, : *Sens. Actuators, B*, vol.149, pp. 301-305.
19. A. Kolmakov, M. Moskovits,: *Annu. Rev. Mater. Res.,* 2004, vol. 34, pp. 151-180.
20. B. Wang, L. F. Zhu, Y. H. Yang, N. S. Xu, and G. W. Yang,: *J. Phys. Chem. C*, 2008, vol. 112, pp. 6643-47.
21. H. T. Wang, B. S. Kang, F. Ren, L. C. Tien, P. W. Sadik, D. P. Norton, S. J. Pearton, and J. Lin,: *Appl. Phys. Lett.*, 2005, vol. 86, pp. 243503-05.
22. H. F. Lu, F. Li, G. Liu, Z. G. Chen, D. W. Wang, H.T. Fang, G. Q. Lu, Z. H. Jiang and H. M. Cheng,: *Nanotechnology*, 2008, vol. 19, pp.405504-10.
23. A. S. Zuruzi, A. Kolmakov, N. C. MacDonald and M. Moskovits,: *Appl. Phys. Lett.,* 2006, vol. 88, pp. 102904-06.
24. H. Liu, D. Ding, C. Ning and Z. Li,: *Nanotechnology*, 2012, vol. 23, pp. 015502-07.
25. M. Buric, K. P. Chen, M. Bhattarai, P. R. Swinehart and M. Maklad,: *IEEE Photonics Technol. Lett*., 2007, vol. 19, pp.255-257.
26., X. Bevenot, A. Trouillet, C. Veillas, H. Gagnaire, and M. Clement,: *Meas. Sci. Technol*., 2002, vol. 13, pp. 118-124.
27. J. Villatoro, D. L. Moreno and D. M. Hernández,: *Sens. Actuators, B*, 2005, vol. 110, pp. 23-27.
28. F. A. Muhammad and G. Stewart,: *Electron. Lett.,* 1992, vol. 28, pp. 1205-06.